Intense Spreading of Radar Echoes from Ionospheric Plasmas

by

Seth E. Dorfman

Submitted to the Department of Physics
in partial fulfillment of the requirements for the degree of

Bachelor of Science

at the

MASSACHUSETTS INSTITUTE OF TECHNOLOGY

June 2005

Author .....
Department of Physics
May 6, 2005

Certified by .....
Min-Chang Lee
Head, Ionospheric Plasma Research Group
Plasma Science and Fusion Center
Thesis Supervisor

Certified by .....
Richard Temkin
Associate Director, Plasma Science and Fusion Center
Department of Physics
Thesis Supervisor

Accepted by .....
David E. Pritchard
Senior Thesis Coordinator, Department of Physics

Intense Spreading of Radar Echoes from Ionospheric Plasmas

by

Seth E. Dorfman

Submitted to the Department of Physics
on May 6, 2005, in partial fulfillment of the
requirements for the degree of
Bachelor of Science

Abstract

On December 25, 2004, a large-scale ionospheric plasma bubble was observed over Arecibo Observatory in Puerto Rico, inducing significant range spreading on ionograms. This phenomena may be explained by means of the $\mathbf{E} \times \mathbf{B}$ instability and gravitational Rayleigh-Taylor instability. A derivation of the dispersion relations for X and O mode waves transmitted from an ionosonde and an analysis of the collisional Rayleigh-Taylor instability leading to an expression for the growth rate are presented as background information. Ray tracing code developed by Nathan Dalrymple, a previous graduate student of Professor Min-Chang Lee, is extended, first to draw refractive index surfaces to illustrate a key principle in ray tracing and later to simulate range spreading due to depleted ionospheric ducts [1]. Data from Arecibo incoherent scatter radar and Arecibo's CADI digisonde is examined showing strong evidence for the development of a plasma bubble following a rise in the plasma layer and the appearance of a horizontal density gradient. In one portion of the ionosphere, this gradient is found to be at an angle of approximately 70 degrees to the Earth's magnetic field, a favorable condition for the excitation of the Rayleigh-Taylor instability over Arecibo.

Thesis Supervisor: Min-Chang Lee
Title: Head, Ionospheric Plasma Research Group
Plasma Science and Fusion Center

Thesis Supervisor: Richard Temkin
Title: Associate Director, Plasma Science and Fusion Center
Department of Physics

Acknowledgments

I would like to especially thank Professor Min-Chang Lee for his support and dedication throughout my three and one half years as an undergraduate research student. My exposure to this one of a kind opportunity helped me develop as a researcher and provided me with a window into the dynamics of the scientific community. I will not soon forget the day we unpacked our optical instrument, the fifteen hour night in the radar control room in Arecibo, the many helpings of both nourishing and intellectual food shared, or the famous diode lecture.

Going well above and beyond his role as a research supervisor, Professor Lee has always advised me based on what he feels is in my best interest, be it in relation to the evolution of this thesis or to my professional development. I also appreciate his continued, generous, and unprecedented support despite my decision to pursue graduate study elsewhere. I have learned much from his unique perspective on both research and personal life over the past three plus years, including the quote that became a staple of my UROP proposals: "The best experimentalist must be a good theoretician."

I would also like to acknowledge all of the other group members for helping to make the last few years both a rewarding and memorable experience. Their hard work, research insights, and sense of humor are to be relished, even in the face of full moons and "electric chickens."

I am also grateful for the support of my thesis co-supervisor, Dr. Richard Temkin.

Finally, I am forever indebted to my parents for their selfless support of my undergraduate study, both personally and financially. I would not be where I am without them and their persistence through the trials of life.

Contents

Chapter 1

X and O Mode Waves

An ionosonde transmits a linearly polarized wave that propagates through the neutral atmosphere and into the ionosphere. Once it reaches the ionosphere, the familiar free-space dispersion relation $\omega = ck$ no longer applies due to the presence of changed particles. Thus, to derive a new dispersion relation, we must consider the presence of these particles and the effect of electric and magnetic fields on their motion. This is done in Sections 4.14-4.15 of [2] which was used to cross check the following alternate derivation.

To derive the dispersion relations for electromagnetic waves in a uniform plasma, we start from Faraday's and Ampere's Laws with the current term retained:

$$\nabla \times \mathbf{E} = -\frac{\partial \mathbf{B}}{\partial \mathrm{t}} \tag{1.1a}$$

$$\nabla \times \mathbf{B} = \mu_0 \mathbf{J} + \mu_0 \epsilon_0 \frac{\partial \mathbf{E}}{\partial \mathrm{t}} \tag{1.1b}$$

Following the normal procedure of differentiating Ampere's Law with respect to time and plugging the result into Faraday's differentiated with respect to space:

$$\nabla \times (\nabla \times \mathbf{E}) = -\mu_0 \frac{\partial \mathbf{J}}{\partial \mathbf{t}} - \mu_0 \epsilon_0 \frac{\partial^2 \mathbf{E}}{\partial \mathbf{t}^2}$$
$$\nabla(\nabla \cdot \mathbf{E}) - \nabla^2 \mathbf{E} = -\mu_0 \frac{\partial \mathbf{J}}{\partial \mathbf{t}} - \mu_0 \epsilon_0 \frac{\partial^2 \mathbf{E}}{\partial \mathbf{t}^2} \tag{1.2}$$

Assuming a small, linear perturbation of the form $\mathbf{E} = \mathbf{E_1} e^{i(\mathbf{k}\cdot\mathbf{r}-\omega t)}$:

$$-\mathbf{k}(\mathbf{k} \cdot \mathbf{E}) + k^2 \mathbf{E} = i\omega\mu_0 \mathbf{J} + \frac{\omega^2}{c^2}\mathbf{E} \tag{1.3}$$

Depending on the angle between $\mathbf{k}$ and $\mathbf{E}$, the first term may cancel. This relationship depends on the relationship between the wave electric field $\mathbf{E}$ and the background (Earth's) magnetic field $\mathbf{B_0}$.

If $\mathbf{E}$ is parallel to $\mathbf{B_0}$, then charged particles affected by the wave electric field will move along the Earth's magnetic field, behaving as if they were in an unmagnetized plasma. In this case, the electromagnetic wave is transverse and the first term drops out of Equation 1.3. For this reason, this wave is known as **ordinary mode** or O-mode. Neglecting thermal motion, the effect of the electric field on electrons may be described by:

$$-e\mathbf{E} = m\frac{\partial \mathbf{v}}{\partial t} = m\frac{1}{n(-e)}\frac{\partial \mathbf{J}}{\partial t}$$
$$\mathbf{E} = \frac{-i\omega m}{ne^2}\mathbf{J} \tag{1.4}$$

Plugging Equation 1.4 into Equation 1.3 yields the dispersion relation:

$$\omega^2 = \frac{ne^2}{\epsilon_0 m} + k^2 c^2 \tag{1.5}$$

Here ${w_{pe}}^2 = \frac{ne^2}{\epsilon_0 m}$ is defined as the the electron plasma frequency.

According to Equation 1.5, as the electron plasma density n increases, an O-mode wave of a given frequency will decrease in wave number. When the wave number reaches zero, the group velocity $\frac{d\omega}{dk} = \frac{kc^2}{\omega}$ also approaches zero, and the wave is

reflected. At this point, the frequency of the wave matches the local plasma frequency as can be clearly seen from Equation 1.5.

The picture looks different for **extraordinary mode** or X-mode waves where $\mathbf{E}$ is perpendicular to $\mathbf{B_0}$. This means that electrons perturbed by the wave must move across the Earth's magnetic field; thus, there is now a significant $\mathbf{E} \times \mathbf{B_0}$ drift. Equation 1.4 must be modified as follows:

$$\begin{aligned} -e\mathbf{E} - e\mathbf{v} \times \mathbf{B_0} &= m\frac{\partial \mathbf{v}}{\partial t} \\ \mathbf{v} \times \mathbf{B_0} &= \frac{i\omega m}{e}\mathbf{v} - \mathbf{E} \qquad (1.6a) \\ \mathbf{v} &= \frac{\mathbf{B_0}}{{B_0}^2} \times (\frac{i\omega m}{e}\mathbf{v} - \mathbf{E}) \\ \mathbf{v} \times \mathbf{B_0} &= \frac{e}{i\omega m}[(\mathbf{E} \times \mathbf{B_0}) - {B_0}^2\mathbf{v}] \qquad (1.6b) \end{aligned}$$

Equating Equations 1.6b and 1.6a:

$$\begin{aligned} \frac{i\omega m}{e}\mathbf{v} - \mathbf{E} &= \frac{e}{i\omega m}[(\mathbf{E} \times \mathbf{B_0}) - {B_0}^2\mathbf{v}] \\ (\frac{i\omega m}{e} + \frac{e{B_0}^2}{i\omega m})\mathbf{v} &= \frac{e}{i\omega m}(\mathbf{E} \times \mathbf{B_0}) + \mathbf{E} \\ \mathbf{v} &= \frac{i\omega\frac{e}{m}}{\frac{e^2{B_0}^2}{m^2} - \omega^2}[\frac{eB_0}{i\omega m}(\mathbf{E} \times \frac{\mathbf{B_0}}{B_0}) + \mathbf{E}] \\ \mathbf{J} = -ne\mathbf{v} &= \frac{i\omega\omega_{pe}^2\epsilon_0}{\omega^2 - {\omega_{ce}}^2}[\mathbf{E} - i\frac{\omega_{ce}}{\omega}\mathbf{E} \times \mathbf{b_0}] \qquad (1.7) \end{aligned}$$

This is the analog of Equation 1.4 for X-mode. Here $\omega_{ce} = \frac{eB_0}{m}$ is the electron cyclotron frequency and $\mathbf{b_0}$ is a unit vector in the direction of the earth's magnetic field. Plugging this result into Equation 1.3:

$$\frac{c^2}{\omega^2}[-\mathbf{k}(\mathbf{k} \cdot \mathbf{E}) + k^2\mathbf{E}] = \frac{\omega_{pe}^2}{\omega^2 - {\omega_{ce}}^2}[i\frac{\omega_{ce}}{\omega}(\mathbf{E} \times \mathbf{b_0}) - \mathbf{E}] + \mathbf{E} \qquad (1.8)$$

Unlike the O-mode case where all the terms in this equation are oriented perpendicularly to the wave vector, in the case of X mode we have both transverse and

longitudinal terms. In order to separate these two parts, let $\mathbf{E_t}$ and $\mathbf{E}_\ell$ be the transverse and longitudinal components of the wave electric field respectively. Equation 1.8 then separates into the following two equations:

$$\frac{c^2}{\omega^2}[-\mathbf{k}(kE_\ell) + k^2\mathbf{E}_\ell] = \frac{\omega_{pe}^2}{\omega^2 - {\omega_{ce}}^2}[i\frac{\omega_{ce}}{\omega}\mathbf{E_t} \times \mathbf{b_0} - \mathbf{E}_\ell] + \mathbf{E}_\ell \tag{1.9a}$$

$$\frac{c^2}{\omega^2}[k^2\mathbf{E_t}] = \frac{\omega_{pe}^2}{\omega^2 - {\omega_{ce}}^2}[i\frac{\omega_{ce}}{\omega}\mathbf{E}_\ell \times \mathbf{b_0} - \mathbf{E_t}] + \mathbf{E_t} \tag{1.9b}$$

Recall that $\mathbf{E}\perp\mathbf{B_0}$ for an X-mode wave. This means that the cross products in Equations 1.9a and 1.9b have magnitudes equal to E_t and E_ℓ respectively. Since $\mathbf{E_t}\perp\mathbf{E}_\ell\perp\mathbf{B_0}$ one of these cross products must pick up a negative sign depending on the coordinate system. Since the final dispersion relation should be coordinate system independent, we shall denote the sign of the first cross product with $\pm$ and the second by $\mp$; these two will eventually cancel.

Noticing that the left hand side of Equation 1.9a equals zero and canceling a unit vector from all terms:

$$\begin{aligned} 0 &= \frac{\omega_{pe}^2}{\omega^2 - \omega_{ce}^2}[i\frac{\omega_{ce}}{\omega}(\pm E_t) - E_\ell] + E_\ell \\ \frac{\omega^2 - \omega_{ce}^2 - \omega_{pe}^2}{\omega^2 - \omega_{ce}^2}(-E_\ell) &= \pm i\frac{\omega_{ce}}{\omega}\frac{\omega_{pe}^2}{\omega^2 - \omega_{ce}^2}E_t \\ E_\ell &= \mp i\frac{\omega_{ce}}{\omega}\frac{\omega_{pe}^2}{\omega^2 - \omega_{pe}^2 - \omega_{ce}^2}E_t \end{aligned} \tag{1.10}$$

Note the factor of i in this expression; this indicates a ninety-degree phase difference between E_t and E_ℓ. Since the relative magnitude of the two components depends on frequency, an X-mode wave in general will be elliptically polarized.

Equation 1.10 is especially interesting when ω^2 approaches $\omega_{ce}^2 + \omega_{pe}^2$; here the ratio $|\frac{E_\ell}{E_t}|$ goes to infinity. When this happens, the X-mode wave is converted into a purely electrostatic upper hybrid wave. For this reason, $\omega_h^2 = \omega_{ce}^2 + \omega_{pe}^2$ is known as the **upper hybrid frequency** and this process is called upper hybrid resonance.

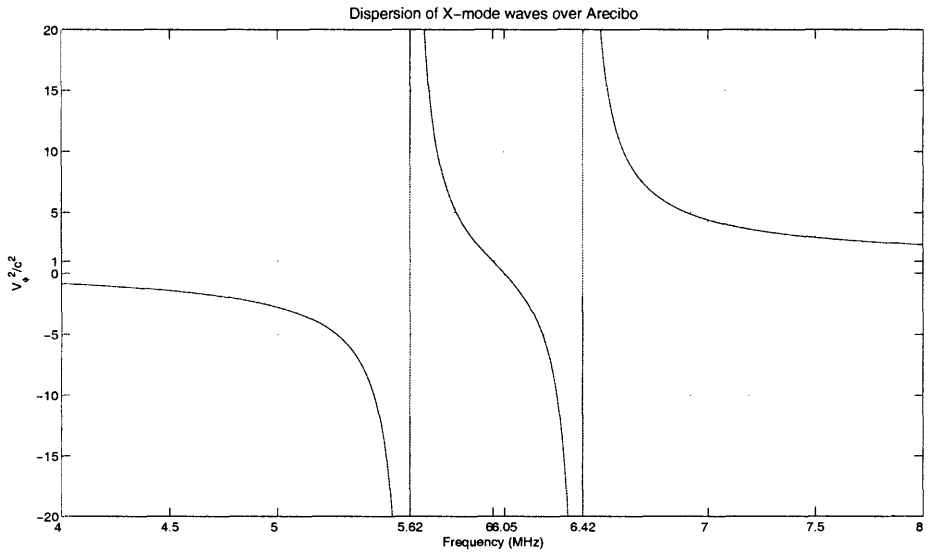

Figure 1-1: Dispersion relation for an X-mode wave with $f_{pe} = 6$ MHz and $f_{ce} = 0.8$ MHz, typical parameters in part of the F layer over Arecibo, Puerto Rico. Under these conditions $f_L = 5.62$ MHz, $f_R = 6.42$ MHz, and $f_h = 6.05$ MHz Based on Figure 4-36 in [2]

Canceling a unit vector from Equation 1.9b:

$$\frac{c^2}{\omega^2}[k^2 E_t] = \frac{\omega_{pe}^2}{\omega^2 - \omega_{ce}^2}[i\frac{\omega_{ce}}{\omega}(\mp E_\ell) - E_t] + E_t \tag{1.11}$$

Substituting Equation 1.10 for E_ℓ and canceling a factor of E_t from all terms:

$$\begin{aligned}
\frac{c^2}{\omega^2}k^2 &= \frac{\omega_{pe}^2}{\omega^2 - \omega_{ce}^2}[i\frac{\omega_{ce}}{\omega}(i\frac{\omega_{ce}}{\omega}\frac{\omega_{pe}^2}{\omega^2 - \omega_{pe}^2 - \omega_{ce}^2}) - 1] + 1 \\
\frac{c^2}{\omega^2}k^2 &= 1 - \omega_{pe}^2\frac{\omega_{pe}^2\omega_{ce}^2 + \omega^2(\omega^2 - \omega_{ce}^2 - \omega_{pe}^2)}{\omega^2(\omega^2 - \omega_{ce}^2)(\omega^2 - \omega_{ce}^2 - \omega_{pe}^2)} \\
\frac{c^2}{\omega^2}k^2 &= 1 - \omega_{pe}^2\frac{(\omega^2 - \omega_{ce}^2)(\omega^2 - \omega_{pe}^2)}{\omega^2(\omega^2 - \omega_{ce}^2)(\omega^2 - \omega_{ce}^2 - \omega_{pe}^2)} \\
\frac{c^2}{\omega^2}k^2 &= 1 - \frac{\omega_{pe}^2}{\omega^2}\frac{\omega^2 - \omega_{pe}^2}{\omega^2 - \omega_h^2}
\end{aligned} \tag{1.12}$$

This is the dispersion relation for the X-mode wave.

As with O-mode, we want to find the conditions under which the X-mode wave

is reflected from the ionosphere. Perhaps the easiest way to do this is to graphically solve Equation 1.12 as shown in Figure 1-1 where the phase velocity ($\frac{\omega}{k}$) of the wave is plotted as a function of frequency. Note that for $\frac{\omega}{2\pi} = f < f_L$ and $f_h < f < f_R$, the phase velocity is negative and the wave can not propagate. As can be seen from the figure, at angular frequencies ω_L and ω_R the phase velocity approaches infinity. These are known as the left-hand and right-hand **cutoff frequencies** and can be found by setting $\frac{\omega}{k}$ to infinity in Equation 1.12:

$$\omega_L = \frac{-\omega_{ce} + \sqrt{\omega_{ce}^2 + 4\omega_{pe}^2}}{2} \tag{1.13a}$$

$$\omega_R = \frac{\omega_{ce} + \sqrt{\omega_{ce}^2 + 4\omega_{pe}^2}}{2} \tag{1.13b}$$

When the plasma density is very small, ω_L is approximately zero and ω_R is approximately ω_{ce}. By comparison, a typical ionosonde transmits frequencies in the range from $1 - 20$ MHz, well above ω_{ce}. As the wave travels upwards, ω_{pe} gradually increases and ω_R grows. When ω_R reaches the frequency of the X-mode wave, the phase velocity of the wave goes to infinity and the wave is reflected. Note that since $\omega > \omega_{ce}$ for ionosonde-produced waves, we need not worry about approaching the left-hand cutoff or upper hybrid resonance, as these frequencies are always less than ω_R. Thus while all three frequencies grow as the plasma density increases, the right-hand cutoff will reach the transmitted frequency first.

Since $\omega_R > \omega_{pe}$, an X-mode wave will be reflected at a lower altitude than an O-mode wave of the same frequency. This can also be seen from Figure 1-1. At the altitude chosen X-mode waves of frequency 6.42 MHz are reflected even though $\frac{\omega_{pe}}{2\pi}$ is only 6 MHz. An O-mode wave of the same frequency would have to travel to a higher altitude before reaching its reflection height. Thus near the reflection height where the uniform plasma approximation used in this chapter applies, a single wave transmitted by an ionosonde can be split into X and O mode components with different dispersion relations; this explains the two traces on an ionogram (see Chapter 4) showing waves of the same frequency reflected at two different altitudes [3].

Chapter 2

Collisional Rayleigh-Taylor Instability

When a dense plasma supports a less dense plasma in the presence of a magnetic field, a small perturbation may grow into a large scale instability. This is illustrated in Figure 2-1. Ions and electrons drift to opposite sides of the perturbation by means of $\mathbf{g} \times \mathbf{B}$ drift. This charge separation creates a self-consistent electric field in the plasma. As shown in the figure, the resulting $\mathbf{E} \times \mathbf{B}$ drift has the effect of amplifying the perturbation. The goal of this section is to derive the growth rate for the instability as done in Section 6.7 of [2], but taking into account collisional effects.

In order to do so, we must first lay out the assumptions that will be made to simplify the problem [3]. First, we will consider a plasma that is macroscopically quasi-neutral and use $n_0 = n_{io} = n_{eo}$ to represent the unperturbed density of both ions and electrons. Second, we consider only low-frequency, large-scale Rayleigh-Taylor modes. Next, we assume that the time scale of ion gyration is much shorter than the other time scales in the problem [3]. This allows us to neglect perturbation frequencies and collision frequencies as small compared to ω_{ci}. Fourthly, we use a cold plasma model (neglecting pressure force) and assume a uniform background Earth's magnetic field and no background electric field. The mass of the electron can be neglected when compared to the mass of the ion; this is substantiated by the fact that the Rayleigh-Taylor instability is driven by gravity which exerts a greater force

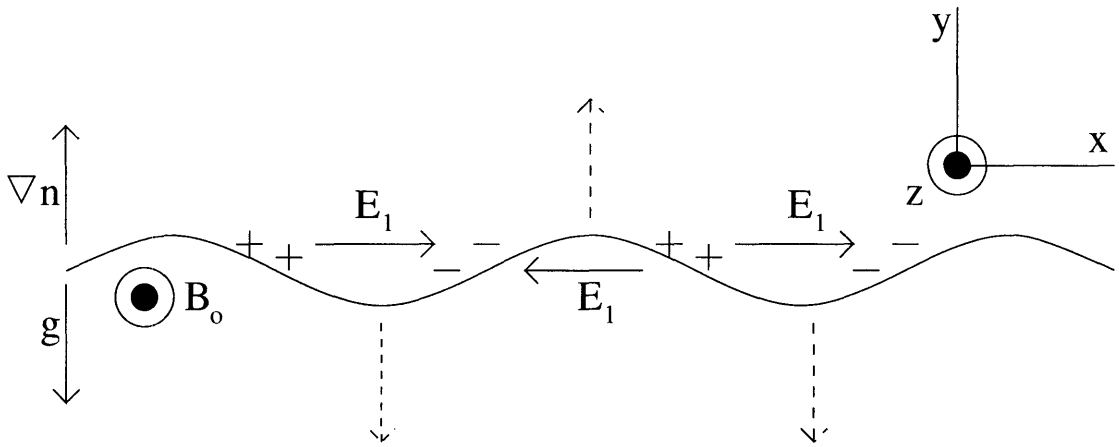

Figure 2-1: The amplification of a small perturbation due to the Rayleigh-Taylor instability. Dashed arrows represent the growth of the instability. Based on [3].

on ions than electrons due to the mass difference of order 10^3.

An important parameter in this derivation is the collision frequency ν_{in}. This frequency represents the momentum relaxation rate of ions due to collisions with neutrals. This can be easily seen by noting that if collisions with stationary neutral particles are the only force acting on the ions, their momentum decays as $e^{-\nu_{in}t}$. To simply the derivation, we will work in the reference frame where the neutral velocity is zero.

Writing the momentum equation for ions:

$$\begin{aligned} Mn_0[\frac{\partial \mathbf{v_0}}{\partial t} + (\mathbf{v_0}\cdot\nabla)\mathbf{v_0}] &= en_0\mathbf{v_0}\times\mathbf{B_0} + Mn_0\mathbf{g} - Mn_0\nu_{in}\mathbf{v_0} \\ M(\mathbf{v_0}\cdot\nabla)\mathbf{v_0} &= e\mathbf{v_0}\times\mathbf{B_0} + M\mathbf{g} - M\nu_{in}\mathbf{v_0} \end{aligned} \tag{2.1}$$

We shall only consider the linear stages of the instability in this chapter. This restricts us to small perturbations of the form $\mathbf{n_1} = \mathbf{n_{1c}}e^{i(\mathbf{k}\cdot\mathbf{r}-\omega t)}$ in the density, velocity and electric field. Note that small here refers to the the amplitude of the perturbation and not the scale length which is assumed to be large. When this perturbation is added to the background parameters, the ion momentum equation may be rewritten as follows:

$$M[\frac{\partial(\mathbf{v_0}+\mathbf{v_1})}{\partial t}+((\mathbf{v_0}+\mathbf{v_1})\cdot\nabla)(\mathbf{v_0}+\mathbf{v_1})] = e[\mathbf{E}+(\mathbf{v_0}+\mathbf{v_1})\times\mathbf{B_0}]+M\mathbf{g}-M\nu_{in}(\mathbf{v_0}+\mathbf{v_1}) \tag{2.2}$$

Here the cancellation of plasma density factor common to all the terms is not shown. Subtracting Equation 2.1 from Equation 2.2:

$$\begin{aligned} M[\frac{\partial \mathbf{v_1}}{\partial t}+(\mathbf{v_0}\cdot\nabla)\mathbf{v_1}] &= e[\mathbf{E}+\mathbf{v_1}\times\mathbf{B_0}]-M\nu_{in}\mathbf{v_1} \\ M[\omega+i\nu_{in}-\mathbf{k}\cdot\mathbf{v_0}]\mathbf{v_1} &= ie[\mathbf{E_1}+\mathbf{v_1}\times\mathbf{B_0}] \end{aligned} \tag{2.3}$$

Let $\alpha = \omega + i\nu_{in} - \mathbf{k}\cdot\mathbf{v_0}$. Solving Equation 2.3 for $\mathbf{v_1}$ using methods similar to those shown in detail in Chapter 1:

$$\mathbf{v_1} = \frac{\omega_{ci}^2}{\omega_{ci}^2-\alpha^2}[\frac{\mathbf{E_1}\times\mathbf{B_0}}{B_0^2}-i\frac{\alpha}{\omega_{ci}}\frac{\mathbf{E_1}}{B_0}] \tag{2.4}$$

Repeating the procedure leading to Equation 2.4 for electrons (Electron parameters which differ from their ion counterparts will carry an additional subscript e.), we obtain for the first order electron velocity:

$$\mathbf{v_{1e}} = \frac{\mathbf{E_1}\times\mathbf{B_0}}{B_0^2} \tag{2.5}$$

Here, the electron mass has been neglected as small compared to the ion mass, setting ω_{ce} to infinity. We can also assume $\omega_{ci}^2 >> \alpha^2 = (\omega-\mathbf{k}\cdot\mathbf{v_0})^2-\nu_{in}^2-2i\nu_{in}(\omega-\mathbf{k}\cdot\mathbf{v_0})$ since the frequency of ion gyration was assumed to be much greater than other frequencies including the collision frequency and Doppler shifted frequency of the perturbation; this greatly simplifies Equation 2.4.

In order to relate Equations 2.4 and 2.5 we need to use the continuity equation for both ions and electrons. Under the quasi-neutrality condition, $n_0 = n_{0i} = n_{0e}$ and $n_1 = n_{1i} = n_{1e}$. The unperturbed equation is:

$$\frac{\partial n_0}{\partial t} + \nabla \cdot n_0 \mathbf{v_0} = 0 \tag{2.6}$$

Linearizing and subtracting zeroth order terms:

$$-i\omega n_1 + i\mathbf{k} \cdot \mathbf{v_0} n_1 + (\mathbf{v_1} \cdot \nabla) n_0 + i n_0 \mathbf{k} \cdot \mathbf{v_1} = 0 \tag{2.7}$$

To write this equation in terms of ion parameters, we refer to Figure 2-1. From here, it is clear that the wavevector $\mathbf{k}$ of the perturbation is along $\mathbf{E_1}$. Also note that $\mathbf{E_1}$ is perpendicular to the density gradient. These two facts allow us to determine which terms in Equation 2.4 cancel when plugged into Equation 2.7 for $\mathbf{v_1}$. Thus, the combined momentum-continuity equation for ions is:

$$\begin{aligned} -i\omega n_1 + i\mathbf{k} \cdot \mathbf{v_0} n_1 + \frac{\mathbf{E_1} \times \mathbf{B_0}}{B_0^2} \cdot \nabla n_0 + n_0 \frac{k\alpha}{\omega_{ci}} \frac{E_1}{B_0} &= 0 \\ (\omega - k v_0) n_1 + i \frac{E_1}{B_0} n_0' + i n_0 \frac{k\alpha}{\omega_{ci}} \frac{E_1}{B_0} &= 0 \end{aligned} \tag{2.8}$$

Here n_0' is the magnitude of the density gradient.

For electrons, Equation 2.1 shows that $\mathbf{v_{0e}} = 0$ if we continue to approximate the electron mass as zero. Thus, plugging Equation 2.5 into Equation 2.7 yields the combined momentum-continuity equation for electrons:

$$\frac{E_1}{B_0} = \frac{i\omega n_1}{n_0'} \tag{2.9}$$

Plugging Equation 2.9 into Equation 2.8, we can immediately eliminate E_1, B_0, and n_1. Performing the substitution and simplifying, we obtain:

$$\omega\alpha = \frac{-v_0 \omega_{ci}}{L} \tag{2.10}$$

Where $L = \frac{n_0}{n_0'}$. From Equation 2.1 with $\mathbf{v_0}$ constant (all derivatives set to zero) and the geometry of Figure 2-1 the scalar v_0 may be written as:

$$v_0 = \frac{g}{\omega_{ci} - \nu_{in}} \tag{2.11}$$

Applying the previously stated approximation $\omega_{ci} >> \nu_{in}$, Equation 2.10 becomes:

$$\begin{aligned} \omega\alpha &= -\frac{g}{L} \\ \omega^2 + \omega(i\nu_{in} - kv_0) + \frac{g}{L} &= 0 \end{aligned} \tag{2.12}$$

Since we assumed a long wavelength perturbation, the kv_0 term may be neglected, leading to the solution:

$$\omega = \frac{-i\nu_{in} \pm \sqrt{-\nu_{in}^2 - \frac{4g}{L}}}{2} \tag{2.13}$$

We take the positive square root since the instability has a positive growth rate. This growth rate γ is given by the imaginary part of the frequency:

$$\gamma = \frac{1}{2}\sqrt{\nu_{in}^2 + \frac{4g}{L}} - \frac{\nu_{in}}{2} \tag{2.14}$$

Chapter 3

Ray Tracing

Chapter 1 considered the simple case of an electromagnetic wave in the ionosphere propagating across the Earth's magnetic field. However, in general ordinary and extraordinary modes may propagate such that the wave vector $\mathbf{k}$ makes a angle θ with $\mathbf{B_0}$ other than $\theta = \frac{\pi}{2}$. In this case, the dispersion relation is given by the Appleton-Hartree formula [2]:

$$c^2\frac{k^2}{\omega^2} = 1 - \frac{2\omega_{pe}^2(1-\frac{\omega_{pe}^2}{\omega^2})}{2\omega^2(1-\frac{\omega_{pe}^2}{\omega^2}) - \omega_{ce}^2\sin^2\theta \pm \omega_{ce}[\omega_{ce}^2\sin^4\theta + 4\omega^2(1-\frac{\omega_{pe}^2}{\omega^2})^2\cos^2\theta]^{\frac{1}{2}}} \quad (3.1)$$

In the special cases discussed in the first chapter $\theta = \frac{\pi}{2}$. Plugging this result into Equation 3.1, we find that the Appleton-Hartree formula reduces to Equation 1.5 or 1.12 depending on which sign is used for $\pm$. Thus, the definitions of ordinary and extraordinary modes may be extended as follows to include cases where θ differs from $\frac{\pi}{2}$: ordinary mode is governed by the Appleton-Hartree formula with a plus sign in the denominator whereas extraordinary mode is governed by the same relation with a minus sign.

Note that if we bring the fraction on the right hand side of Equation 3.1 to the left, the dispersion relation takes on the form [4]:

$$D(x, y, z; n_x, n_y, n_z) = C \quad (3.2)$$

Here C is a constant that does not depend on any of the six variables. While these variables do not explicitly appear in Equation 3.1, ω_{pe} will vary with altitude in the ionosphere depending on the local plasma density, ω_{ce} and ω may be taken as constant, $n^2 = c^2\frac{k^2}{\omega^2}$, and the angle θ depends on the direction of the vector $\mathbf{n} = (n_x, n_y, n_z)$.

This general form for the dispersion relation is instrumental to deriving a set of equations that may be used to trace the path of a ray as it propagates from the neutral atmosphere into the ionosphere following the approach outlined in Section 14.3 of [4]. A dispersion relation written in the form of Equation 3.2 defines what is known as a **refractive index surface**. For given values of x, y, and z, this surface is simply the curve given by Equation 3.2 drawn on the n_x, n_y, and n_z axes.

Note that in Equation 3.1 the only dependence on the spacial coordinates is through ω_{pe}. This means that the refractive index surfaces can be easily labeled by the value of ω_{pe}. However, it is often easier to define a new dimensionless quantity $X = \frac{\omega_{pe}^2}{\omega^2}$ and label the surfaces in this manner. Thus, for the ordinary mode wave, $X = 0$ represents no plasma and $X = 1$ represents the plasma density at the reflection height. Two different cross sections of several surfaces for ordinary mode are shown in Figure 3-1.

The key principle in ray tracing is that the wave propagates in the direction normal to the refractive index surface (a proof is shown in Appendix A.2). Note that in the ionosphere this may be different from the direction of the wave normal as defined by $\mathbf{n}$. If $n_y = 0$ as is the case on the left hand side of Figure 3-1, the direction of the ray at any point may be found by first locating the values of n_x and n_z at that point on the plot. If the x and z axes are drawn on top of the n_x and n_z axes, the direction of the wave at the point in question is that of the the normal vector to the refractive index surface in the x-z plane.

Now let the vector $\mathbf{V} = (\frac{dx}{dt}, \frac{dy}{dt}, \frac{dz}{dt})$ represent the wave velocity [4]. Since $\mathbf{V}$ is normal to the refractive index surface, we can use the fact that the gradient of a vector field is perpendicular to the surfaces of constant potential to write:

$$\mathbf{V} = (\frac{dx}{dt}, \frac{dy}{dt}, \frac{dz}{dt}) = A(\frac{\partial D}{\partial n_x}, \frac{\partial D}{\partial n_y}, \frac{\partial D}{\partial n_z}) \tag{3.3}$$

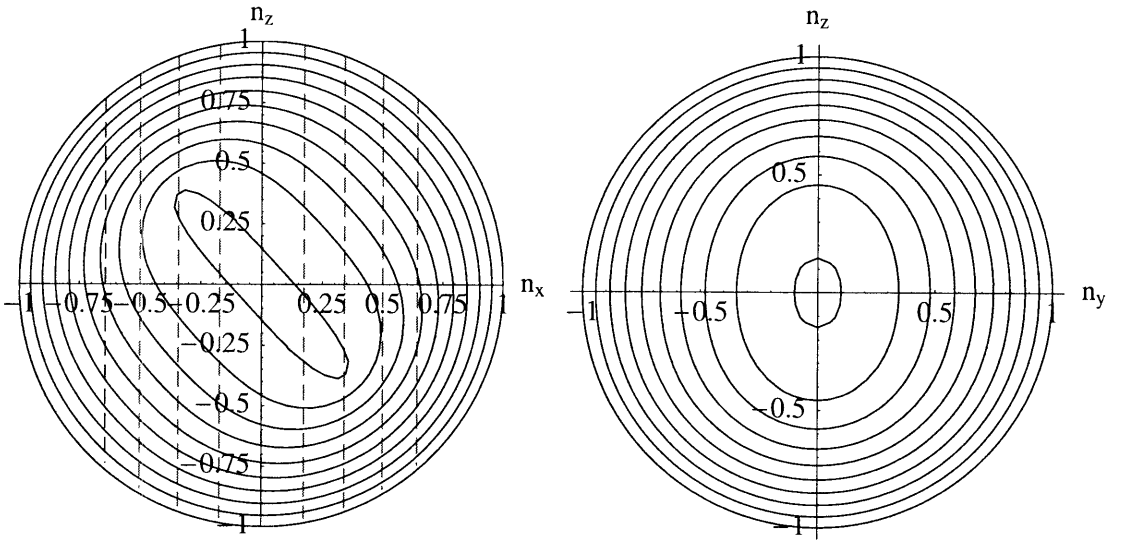

Figure 3-1: Cross sections of refractive index surfaces for ordinary mode for $n_y = 0$ and $n_x = 0$ respectively with the Earth's magnetic field at a 47.5 degree declination angle in the x-z plane. Sequential curves range from the outermost with $X = 0$ to the innermost with $X = 0.99$ in increments of 0.11.

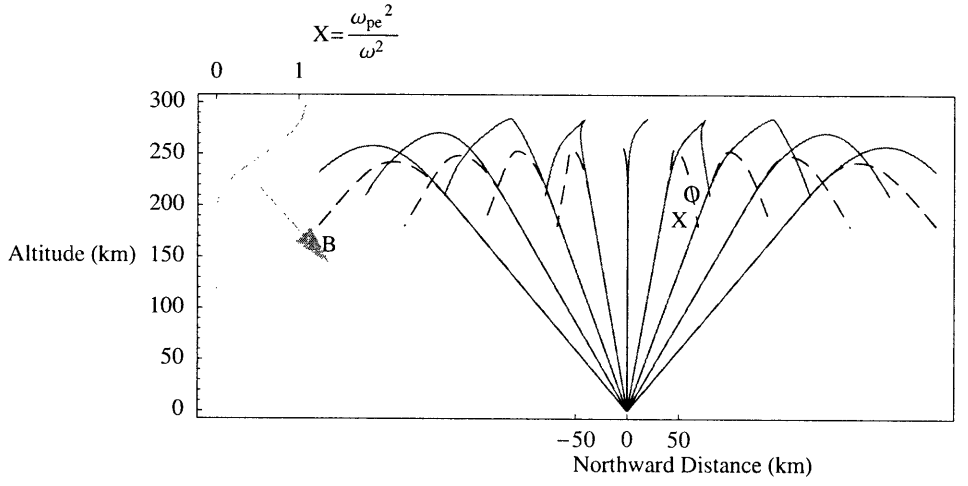

Figure 3-2: Path of O (solid lines) and X (dashed lines) modes at angles of incidence ranging from -40 degrees to 40 degrees in 10 degree increments transmitted in the x-z plane. The ray paths are shown as dashed lines in refractive index space in figures 3-1 and 3-3. The plasma density profile model with an F peak at 300 km is shown on the left. Generated by [1].

Where A is a constant that may be found by plugging the right hand side of the equation into the relation $\mathbf{V} \cdot \mathbf{n} = c$:

$$A = \frac{c}{n_x \frac{\partial D}{\partial n_x} + n_y \frac{\partial D}{\partial n_y} + n_z \frac{\partial D}{\partial n_z}} \tag{3.4}$$

Equation 3.3 gives us only three differential equations for six unknowns. To derive the other three, consider an infinitesimal displacement in space δx. Over such a distance, D from Equation 3.2 must remain constant. Since y and z do not change, we can use the chain rule to write [4]:

$$\frac{\delta D}{\delta x} = \frac{\partial D}{\partial x} + \frac{\partial D}{\partial n_x}\frac{\partial n_x}{\partial x} + \frac{\partial D}{\partial n_y}\frac{\partial n_y}{\partial x} + \frac{\partial D}{\partial n_z}\frac{\partial n_z}{\partial x} = 0 \tag{3.5}$$

It can be shown from Maxwell's equations that for a progressive wave (a wave in which the wave impedance is independent of spacial coordinates) $\nabla \times \mathbf{n} = 0$ (see Appendix A.1). Thus, $\frac{\partial n_y}{\partial x} = \frac{\partial n_x}{\partial y}$ and $\frac{\partial n_z}{\partial x} = \frac{\partial n_x}{\partial z}$ in Equation 3.5:

$$0 = \frac{\partial D}{\partial x} + \frac{\partial D}{\partial n_x}\frac{\partial n_x}{\partial x} + \frac{\partial D}{\partial n_y}\frac{\partial n_x}{\partial y} + \frac{\partial D}{\partial n_z}\frac{\partial n_x}{\partial z} \tag{3.6}$$

Now, using the results from Equation 3.3:

$$\begin{aligned} 0 &= A\frac{\partial D}{\partial x} + \frac{dx}{dt}\frac{\partial n_x}{\partial x} + \frac{dy}{dt}\frac{\partial n_x}{\partial y} + \frac{dz}{dt}\frac{\partial n_x}{\partial z} \\ 0 &= A\frac{\partial D}{\partial x} + \frac{dn_x}{dt} \end{aligned} \tag{3.7}$$

Repeating this procedure for a small displacement in the y and z directions, we obtain the set of equations [4]:

$$\left(\frac{dn_x}{dt}, \frac{dn_y}{dt}, \frac{dn_z}{dt}\right) = -A\left(\frac{\partial D}{\partial x}, \frac{\partial D}{\partial y}, \frac{\partial D}{\partial z}\right) \tag{3.8}$$

Equations 3.3 and 3.8 represent a set of six differential equations that along with initial conditions and the appropriate dispersion relation may be solved to determine the ray path in the ionosphere. This was done with Mathematica (see Appendix B.2)

to produce Figure 3-2 [1].

One can gain an intuitive feeling for the expected solution to these equations by returning to the idea of the refractive index surface from which they were derived. In Figure 3-1 the dashed lines drawn on the the refractive index surface represent ray paths in n-space for the coordinate-space paths shown in Figure 3-2.

When a ray leaves the ionosonde, $\omega_{pe} = 0$, $n_z > 0$, and the ray is on the refractive index surface marked by the unit circle. The angle from the vertical direction at which the ray is transmitted is equivalent to the angle from the n_z axis in Figure 3-1 at which the trace for that ray begins. As the ray moves into the ionosphere, n_z decreases and the direction of the ray in coordinate space changes such that it is always perpendicular to the refractive index surface at the point in question.

Looking at the figure, some of the ray paths are tangent to a refractive index surface at one point, while others are not. At this tangent point, if it exists, the ray is directed horizontally and reflection occurs even though the wave may be below the O-mode reflection height found in Chapter 1. If such a point does not exist, then the O-mode wave reflects when it reaches the line where $X = 1$. As shown in Figure 3-2 this results in a cusp at the reflection height for small transmission angles since the ray is never directed horizontally.

A similar diagram for X mode is shown in Figure 3-3. Note that the surfaces shrink to a point rather than a line in both cross sections; this means that the ray path of X mode does not include cusps at the reflection height. Also, note that the curves do not approach $X = 1$. Instead, they vanish at $X = 1 - \frac{\omega_{ce}}{\omega}$ where the plasma frequency corresponds to the wave frequency of the right-hand cutoff given in Equation 1.13b.

Some interesting refractive index surfaces for X mode may be obtained if we choose values for the wave frequency that are less than the electron cyclotron frequency. These are shown in Figure 3-4. As n_z changes with increasing altitude, the shapes of these curves allow for more than one tangent point. In addition, the curves do not shrink to a line or point at $\omega = \omega_{pe}$, allowing for higher reflection heights and more complicated ray paths.

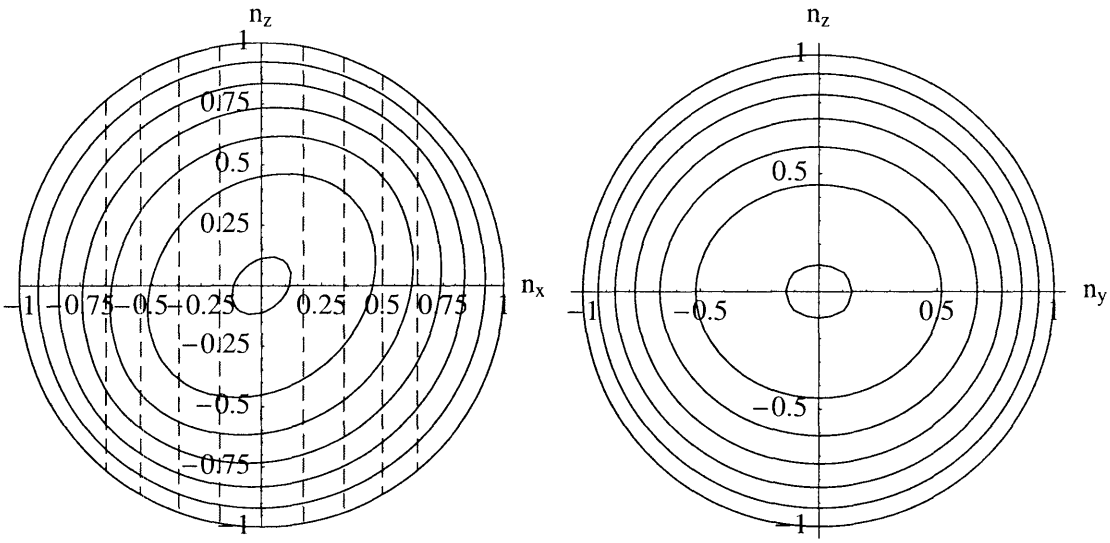

Figure 3-3: Cross sections of refractive index surfaces for extraordinary mode for $n_y = 0$ and $n_x = 0$ respectively with the Earth's magnetic field at a 47.5 degree declination angle in the x-z plane. Sequential curves range from the outermost with $X = 0$ to the innermost with $X = 0.66$ in increments of 0.11. $\frac{\omega_{ce}}{\omega} = 0.3334$.

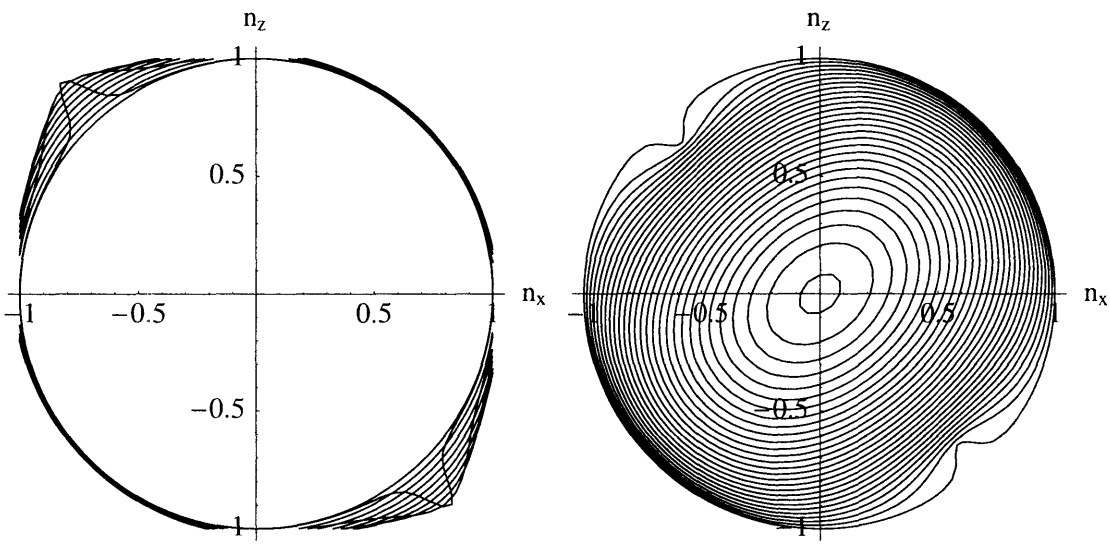

Figure 3-4: Cross sections of refractive index surfaces for extrordinary mode when $n_y = 0$ and $\omega < \omega_{ce}$. The left plot shows surfaces for $\omega < \omega_{pe}$ while the right plot shows surfaces for $\omega > \omega_{pe}$. The Earth's magnetic field is the same as in Figure 3-3.

Chapter 4

Arecibo Experiments

Experiments aimed at observing naturally occurring plasma turbulence were carried out at Arecibo Observatory from August 13-21, 2004 and again from December 20-27, 2004. Diagnostics used include Arecibo's Canadian Advanced Digital Ionosonde (CADI) and Arecibo Incoherent Scatter Radar (ISR). These experiments were inspired in part by 1997 experiments that made use of a now-disbanded HF heater to generate artificial plasma turbulence that was observed with ISR [5].

The CADI Digisonde, deployed and run by the observatory, was set up to record data every five minutes. The digisonde is a swept frequency HF radar that transmits frequencies between 1 MHz and 20 MHz. Based on the transit time and a propagation speed of c, the **virtual heights** of the X and O mode echoes are plotted against frequency. This plot, known as an **ionogram**, was used to determine if the ionosphere was quiet or turbulent during our experiments.

Arecibo 430 MHz ISR produced plots of the plasma density profile using incoherent scatter techniques. The radar is a spherical dish 305 meters in diameter with a linefeed located at the focal line to transmit and collect the radiation. Because the dish is spherical, the radar beam is steerable; it was operated in both vertical and rotating modes during our experiments. In the later mode, the beam was at an angle of 15 degrees from the zenith and completed a circular path on average once every 15 minutes and 46 seconds as shown in Figure 4-1. Each rotation period is represented by an arrow at the bottom of Figure 4-2. A forward arrow indicates

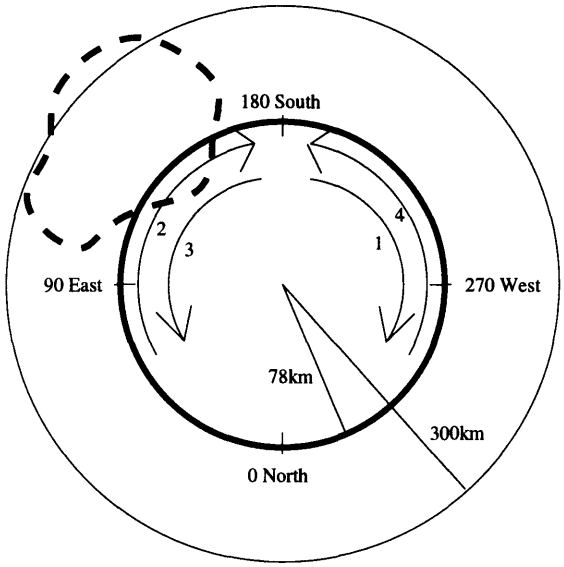

Figure 4-1: Cartoon showing a horizontal cross section of the ionosphere at an altitude of 300 km. The dark blue circular sliver shows the area diagnosed by the rotating Arecibo ISR; the lightly shaded pink region shows the additional area diagnosed by Arecibo CADI. Directional numbered arrows represents the order in which ISR scans the dark region. The path shown represents two full rotations. The dark dashed line indicates a region where a plasma bubble is located.

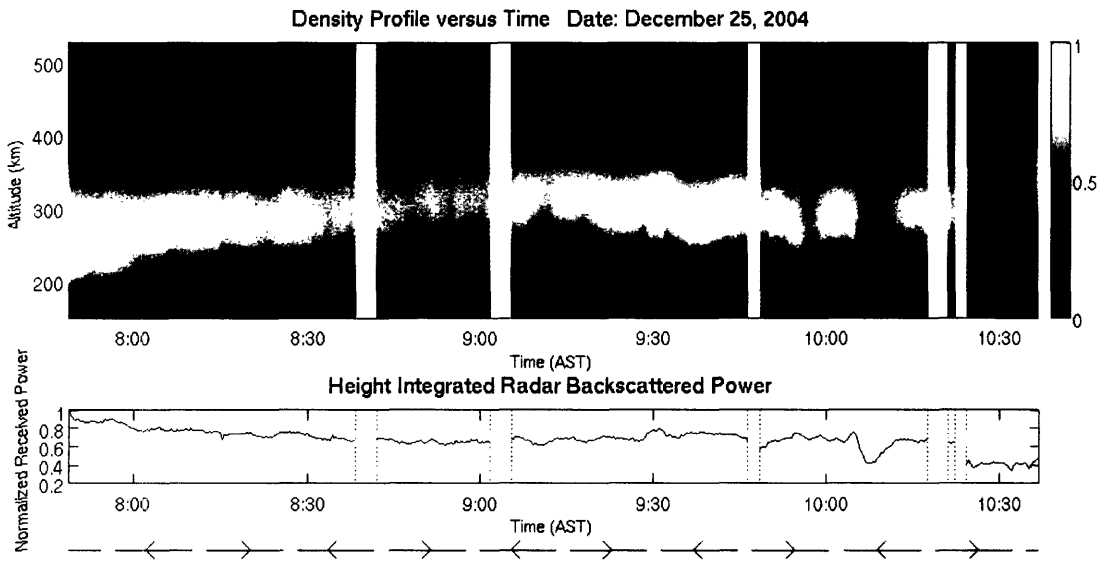

Figure 4-2: Range-Time-Intensity plot for December 25, 2004. Power is integrated over the 150 to 525 kilometer range shown in the top plot and normalized with respect to the highest value shown.

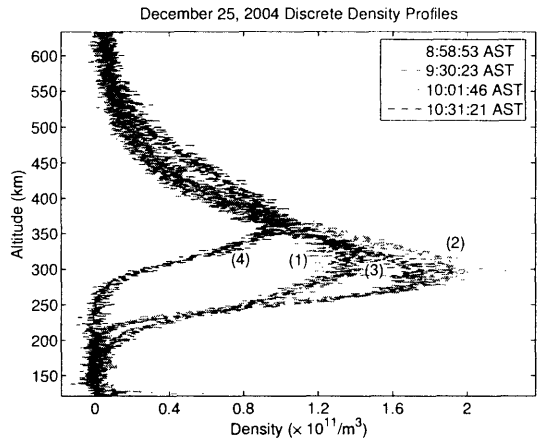

Figure 4-3: Discrete density profiles taken on December 25, 2004 when the radar is pointed south (1) as the plasma layer finishes rising, (2) when the layer descends slightly, inducing a sharp density gradient on the bottomside, (3) when a plasma bubble begins to develop in an adjacent region, and (4) during the development of a plasma bubble in the south.

that the region to the southeast is scanned just before the radar reverses direction; a backward arrow indicates that the last region scanned is to the southwest. With a very narrow beamwidth of 0.16 degrees, the radar diagnoses a very small region of the ionosphere. By contrast, CADI's 90 degree beamwidth covers the entire region spanned by ISR.

Results from ISR are shown in Figure 4-2. The top panel is a range-time-intensity (RTI) plot, it shows the intensity of the backscattered radar echo plotted against time and altitude. As seen from the plot, the F region plasma layer rises steadily from 8:00PM to 9:15PM Atlantic Standard Time (AST). Later on in the night, depleted regions known as **plasma bubbles** develop. Note that successive pieces of data are taken from different regions of the ionosphere as the beam rotates, stops, reverses direction and repeats. Thus, the sudden rise in the plasma layer and corresponding decrease in intensity occurs as the beam enters a region where a plasma bubble is located such as the one bounded by dashed lines in Figure 4-1. The five gaps in the radar data indicate times when the radar was either not operating due to instrumentation problems or being used in a different operational mode for other

measurements.

The bottom plot shows the normalized backscattered power, an approximation for the relative total electron content (TEC) of the ionosphere. This approximation holds because $P \sim \frac{n_e}{1+\frac{T_e}{T_i}}$ where P is the power reflected from any one point, n_e is the electron density, and T_e and T_i are the electron and ion temperatures respectively. Since the later two quantities are not expected to vary much with altitude and time, relative values of the integral of P well-represent integrals of n_e over altitude [5]. Note that the TEC decreases by nearly a factor of two when the radar beam enters a bubble.

Figure 4-3 shows discrete density profile cross sections of the RTI plot when the radar beam is at its turnaround point after approaching from the east. The four profiles shown are taken at four key times as explained in the caption.

Some corresponding ionograms from Arecibo CADI are shown in Figure 4-4. The gradual rise in the plasma layer is clearly visible in the ionograms taken between 7:45PM and 8:00PM AST. These ionograms show the higher-frequency portions of the trace rising first followed by the low frequency portions. This is confirmed by Figure 4-2 which shows that the altitude of the peak plasma density rises between 7:45PM and 8:00PM AST although the whole layer does not start to rise until 8:00PM.

Spread F, the spreading of ionosonde traces due to non-quiescent ionospheric conditions, begins to develop on CADI at around 8:55PM but then dies out at around 9:20PM when the plasma layer on the RTI stops rising. As the layer descends slightly, a modulation of the lower portion is visible on the RTI, indicating the presence of a horizontal density gradient.

At 9:45PM the ionogram shown in Figure 4-5 shows an additional interesting feature. At the top of CADI's range near 484 kilometers, the ionogram shows what somewhat resemble spread X and O mode traces. Often, a second set of traces or **second hop** occurs when the signal from the ionosonde reflects from the ionosphere, is bounced back from the ground, and reflects off the ionosphere again before reaching the receiver. In this case, the second set of traces will appear at twice the altitude of the first. However, the feature at a virtual height of 450 km in the 9:45PM ionogram is

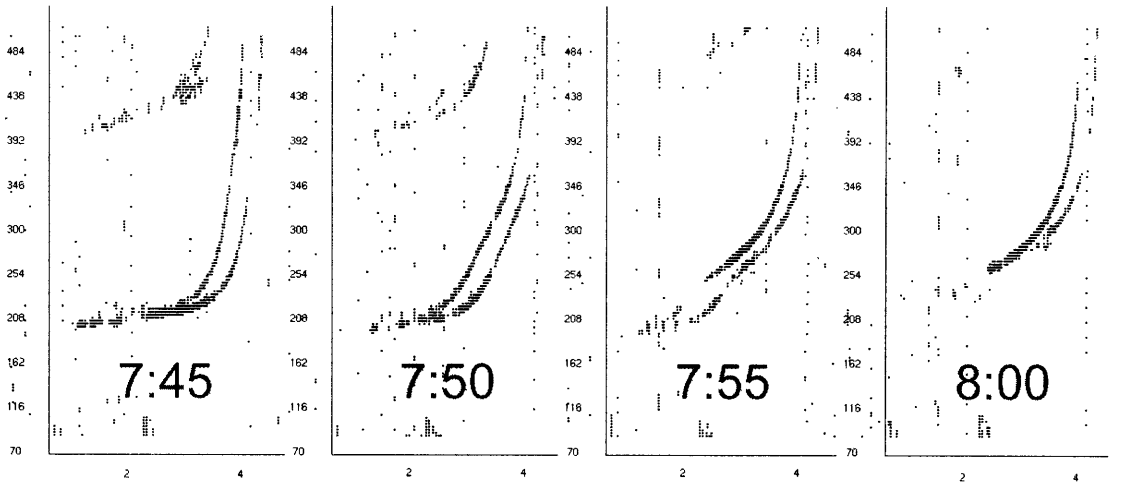

Figure 4-4: Ionograms between 7:45PM and 8:00PM AST showing a rising plasma layer. Transmitted frequency (on a log scale) is plotted against virtual height. Dark areas indicate reflected signal.

not at twice the altitude of the X and O mode traces. Furthermore, as time advances, much clearer spread traces appear at a lower altitude as well. Meanwhile, the X and O mode traces fade; by 10:20PM the ionogram shows one set of traces spread in altitude starting at a virtual height of 300 km.

The high-altitude spread traces correspond to the time period that plasma bubbles are seen on ISR. When the bubbles are only in a part of the region spanned by the rotating radar (9:55PM-10:15PM), both the normal traces and higher spread traces are seen on the ionograms. However, when the bubble completely predominates around 10:25PM only the spread traces are seen. A similar phenomena was observed on December 26, 2004; digisonde and radar data for this event is presented in [6] and [7].

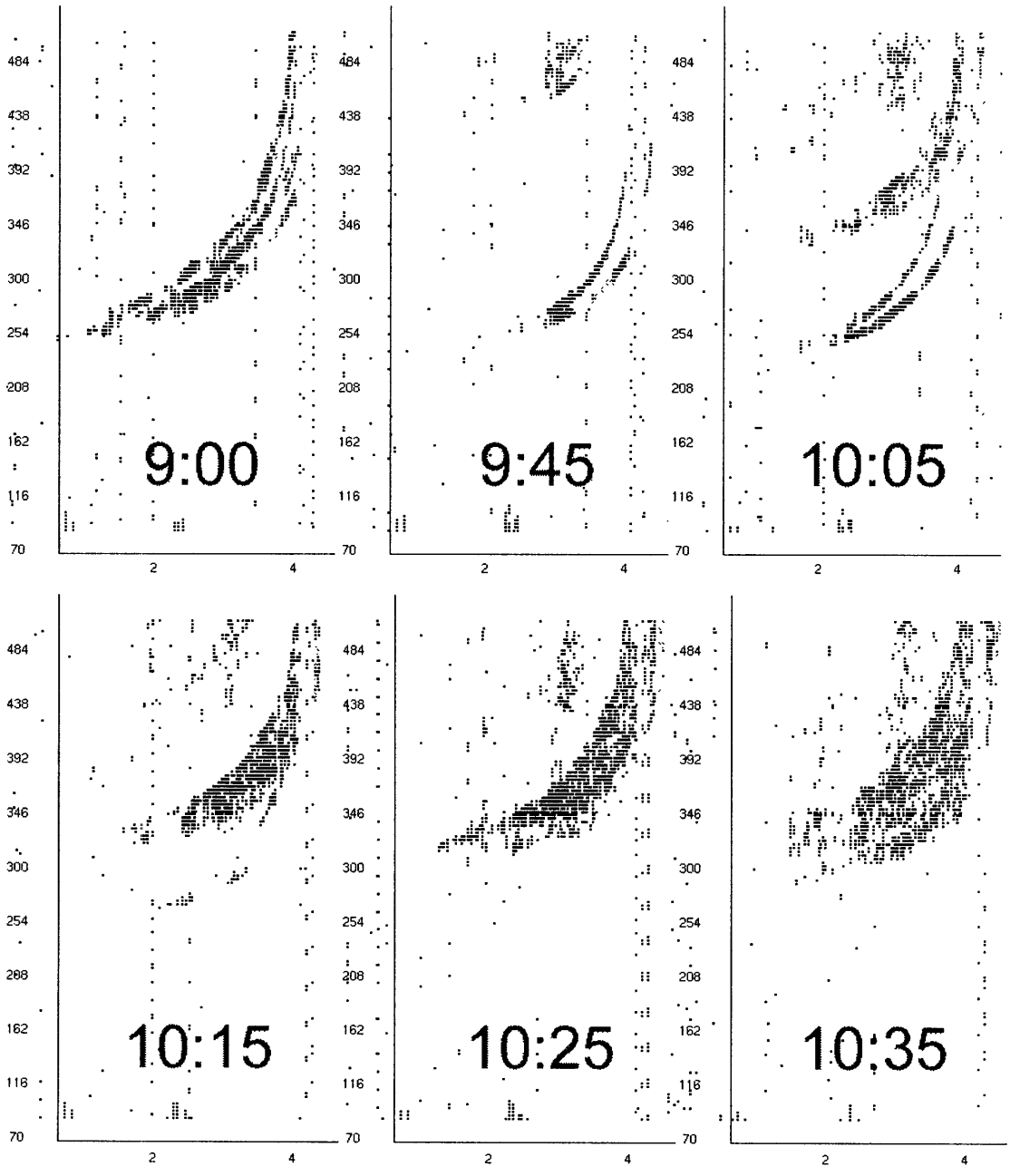

Figure 4-5: Ionograms recorded during light spread F (9:00PM) and plasma bubbles (others). Axes are the same as Figure 4-4.

Chapter 5

Ray Tracing in the Presence of Ducts

The ray tracing principles discussed in Chapter 3 may be used to trace the path of rays in Mathematica (see Appendix B.1) with several ionospheric models. Shown on the left hand side of Figure 5-1 is the basic ionospheric model known as the **Chapman layer**. This shape is a very good approximation of the ionosphere that may be obtained by modeling the plasma production, transport, and recombination processes at work. When this model is used, the ray tracing equations produce the linear traces shown on the right hand side of Figure 5-1. This graph shows transmitted frequency versus number of steps for half of a round trip from the transmitter to ionosphere

Degree Range	$\frac{\delta n}{n} = 0.02$, O mode	$\frac{\delta n}{n} = 0.02$, X mode	$\frac{\delta n}{n} = 0.05$, O mode	$\frac{\delta n}{n} = 0.05$, X mode
-45 to -35	30	25	45	55
-35 to -25	1	11	13	26
-25 to -15	20	10	13	24
-15 to -5	34	14	42	18
-5 to 5	9	5	8	19
5 to 15	2	11	4	7
15 to 25	0	0	0	0
25 to 35	0	0	0	0
35 to 45	0	0	0	0

Table 5.1: Number of rays that land within one kilometer of the transmitter for different duct sizes as a function of transmitted angle.

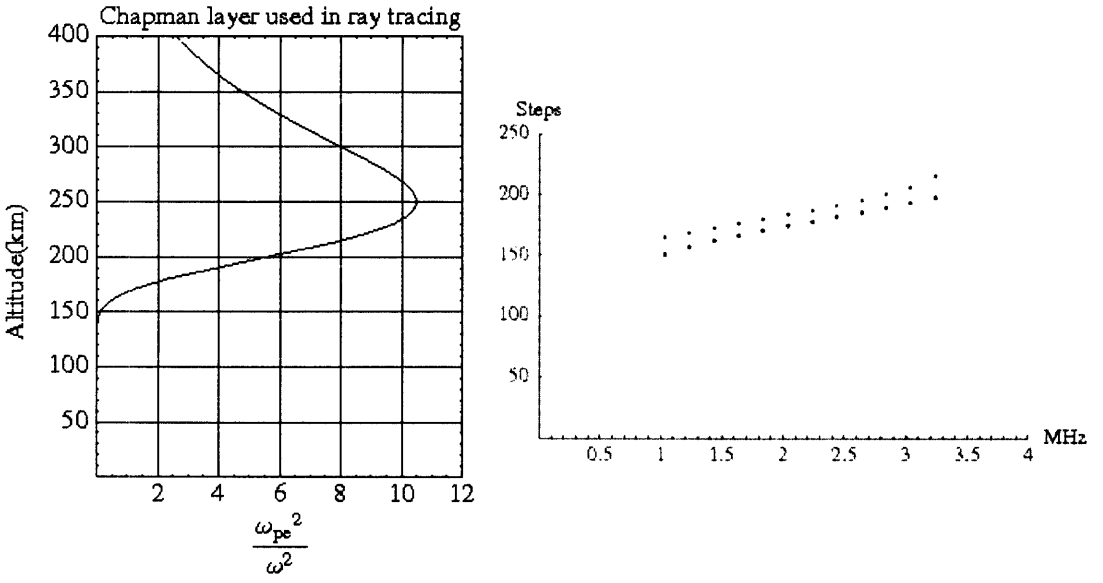

Figure 5-1: Chapman layer model used in this chapter for a quiet ionosphere with $\omega = 2\pi$ radians per second (left). Ray tracing results for this model (right). O mode echoes are shown in red; X mode echoes are in blue.

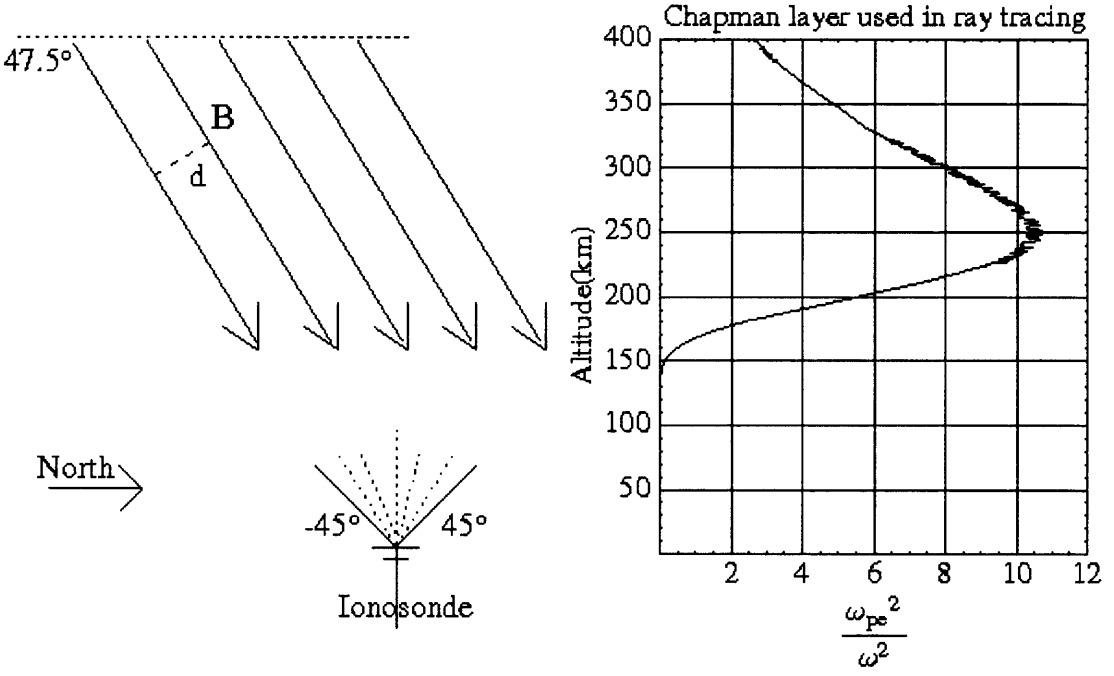

Figure 5-2: Cartoon showing magnetic ducts in the x-z plane (left). Chapman layer from Figure 5-1 with magnetic ducts included such that $\frac{\delta n}{n} = 0.02$ (right). The scale length d was set to 300 m for all simulations in this chapter.

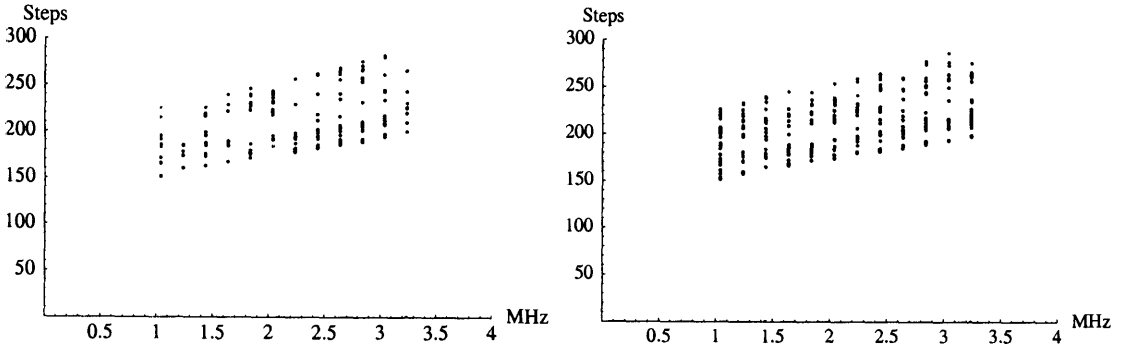

Figure 5-3: Ray tracing results showing spread F. The results on the left are for $\frac{\delta n}{n} = 0.02$ while the results on the right are for $\frac{\delta n}{n} = 0.05$. Only rays which return to the ground within 1 kilometer of the transmitter are graphed. O mode echoes are shown in red; X mode echoes are in blue.

and back; one step is roughly equivalent to the time it takes a ray to travel a distance of one kilometer in the free space below the ionosphere. The computer-simulated ionosonde transmits frequencies from 1.0373 MHz to 3.2373 MHz (just below the peak plasma frequency) in increments of 0.2 MHz. The ionosonde has a beam width extending from -45 to 45 degrees run in increments of 0.5 degrees.

Now, add field-aligned density fluctuations known as **magnetic ducts** to the model as shown in Figure 5-2. The ducts are characterized by a scale length d that defines the spacial variation of the density fluctuation across the field lines and a ratio $\frac{\delta n}{n}$ of the perturbation to the background plasma density.

Under these conditions, the ray no longer encounters a horizontally stratified ionosphere and the reflection height varies sinusoidally as a function of x. Rays launched with a significant component along the magnetic field direction may be trapped in the ducts and reflected in various directions; some return to the transmitter significantly delayed. This is confirmed by Table 5.1 in which the computer-generated rays that return to the transmitter are categorized with respect to their transmission angle. As expected from this geometry, many more rays launched into the magnetic ducts (negative angles) return to the transmitter than those launched across the ducts (positive angles). However, a real-world receiver cannot determine the direction from which the rays were launched. Thus delayed rays and non-delayed rays are superimposed on the ionogram in Figure 5-3. Delayed rays are interpreted as reflecting from a higher

altitude; thus the traces appear spread vertically as shown in the figure. Comparison of the two datasets suggestions that a larger $\frac{\delta n}{n}$ leads to more trapped rays and hence more intense spreading.

This idea may also be extended to configurations other than ducts. For example, rays may also become trapped in a depleted plasma bubble and undergo multiple reflections within the bubble before retuning to the ground. This delaying processes nicely explains the spread traces at high altitudes discussed in Chapter 4. There are no traces between the clear traces and the spread second hop because the rays are either trapped for a while or reflect normally; none are delayed by only a small amount.

Chapter 6

Discussions and Conclusions

The data discussed in Chapter 4 may be explained in terms of the interaction of two plasma instabilities. They are the Rayleigh-Taylor instability discussed in Chapter 2 and the $\mathbf{E} \times \mathbf{B}$ instability.

The $\mathbf{E} \times \mathbf{B}$ instability is typically preceded by the **dynamo effect** in which a neutral wind drags along ions, separating them from electrons and creating a DC electric field. If this field is in the eastward direction, the $\mathbf{E} \times \mathbf{B}$ direction will be upward, forcing the entire plasma layer up. This effect can be clearly seen in the RTI data from Figure 4-2 from 8:00PM to 9:15PM AST.

The light spread F shown at around 9:00PM AST compares favorably with the result of computer simulations of magnetic ducts presented in Chapter 5. As the plasma drifts upward under the influence of $\mathbf{E} \times \mathbf{B}$ its motion is constrained by the Earth's magnetic field lines. This allows for the development of a small variation in density among adjacent flux tubes–precisely the model used in the simulations.

Following this rise, a little after 9:30PM a rectangular modulation may be seen in the bottomside of the F layer while the radar is pointed south. This modulation is shown in more detail in Figure 6-1. As seen from the figure, regions with the same plasma density vary in altitude by about 20 kilometers over the range swept out by the radar. According to this picture, the region of lowest plasma density exists in the southeast. As described in the preceding chapter, the Rayleigh-Taylor instability is favorably excited when the density gradient is perpendicular to the magnetic field.

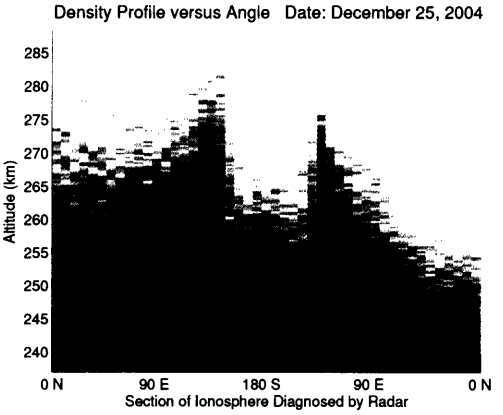

Figure 6-1: Closeup view of the modulations on the bottomside of F layer at around 9:30PM AST. The time axis has been relabeled to show the region of the ionosphere being diagnosed by the radar.

Since a component of the density gradient observed in Figure 6-1 is in the meridional plane, there is a chance for this horizontal gradient, when added to the background vertical gradient, to produce a net gradient at a near-perpendicular angle to the magnetic field [3]. To create this favorable geometry at Arecibo, the more dense region would have to be toward the north. In other words, the density gradients centered at about 90 degrees in the figure is ideal for the favorable excitation of the Rayleigh-Taylor instability.

It is also interesting to note how this "northern" density gradient differs from the sharper "southern" density gradient that forms the edges of the rectangular bulge in the center of the figure. Although the southern gradient is sharper, it produces a net density gradient more aligned with the magnetic field, suppressing the instability. By contrast, if we estimate from the figure that the northern gradient occurs over approximately 45 degrees of the radar sweep, the horizontal scale of the gradient at an altitude of 255 km may be calculated at about 54 km. When this calculation is combined with the estimate of 20 km for the vertical extent of the gradient, we obtain an angle of approximately 70 degrees between the net density gradient and the Earth's magnetic field, a more favorable condition for the excitation of the Rayleigh-Taylor instability than that given by the declination angle of 47.5 degrees during quiescent

conditions at Arecibo.

Half of an hour later, a large-scale plasma bubble develops in roughly the same region, but slightly further north. Thus the center of the bubble is determined not by the area of the lowest plasma density in Figure 6-1 but by the area where the northern density gradient is strongest.

A slight drop in the F layer following the $\mathbf{E} \times \mathbf{B}$ induced rise may have also helped trigger the Rayleigh-Taylor instability. If we include the motion of the neutrals by adding a factor of $Mn_0\nu_{in}v_n$ (where v_n is the neural velocity) in Equation 2.1, the factor of $\nu_{in}v_n$ may be added to the gravity $\mathbf{g}$ to produce an effective gravity term. This means that downward motion of the neutrals has a similar effect as increasing gravity; in both cases the growth rate given in Equation 2.14 in enhanced. As shown in Figure 4-3, the density gradient becomes sharper during this period also increasing the instability growth rate. Thus, the plasma bubbles that begin to form to the south at 10:00PM are a triggered in part by the descent in the plasma layer in the same region at 9:30PM.

The ionograms confirm the presence of a plasma bubble during the time that the Rayleigh-Taylor instability is expected to predominate. Around 10:00PM, when the large-scale plasma bubble first develops, the presence of both quiet and spread traces indicates that both quiescent regions and turbulent regions with field-aligned density perturbations simulated in Chapter 5 are present. When the entire region spanned by ISR is predominately turbulent toward the end of the data sample, only spread traces are seen.

Bibliography

[1] N. Dalrymple (a previous PhD student of Prof. Min-Chang Lee) "Ray Tracing Code" (2002).

[2] F. Chen, *Introduction to Plasma Physics and Controlled Fusion* (Plenum Press 1984).

[3] Consultation with Professor Min-Chang Lee (2005).

[4] K. Budden, *The Propagation of Radio Waves* (Cambridge University Press 1985).

[5] M. C. Lee, et al, *Geophysical Research Letters* **26** 37-40 (1999).

[6] M. C. Lee, S. E. Dorfman, et al, "Remote Sensing of Ionospheric Plasma Turbulence at Arecibo." Ionospheric Interactions Workshop, Santa Fe, NM, 4/18/2005.

[7] M. C. Lee, S. E. Dorfman, et al, "Observations of Naturally-Occurring Ionospheric Plasma Bubbles at Arecibo." *Geophysical Research Letters* In Preparation (2005).

Appendix A

Ray Tracing: Derivation Appendix

A.1 Curl of the Refractive Index

The curl of the refractive index for a progressive wave is zero. To show this, let's use the waveform:

$$\mathbf{E} = \mathbf{E_1} e^{i[k_0(f(\mathbf{r}))-\omega t]} \tag{A.1}$$

Here k_0 is the free space wavenumber and $f(\mathbf{r})$ is the spacial dependence of the wave; the refractive index is defined such that $\mathbf{n} = \nabla f(\mathbf{r})$ is the refractive index vector described in Chapter 3. The magnetic field of the wave has a similar waveform such that $\frac{\mathbf{E}}{\mathbf{B}} = \frac{\mathbf{E_1}}{\mathbf{B_1}}$ does not depend on any spacial coordinates, satisfying the requirement for a progressive wave [4].

Substituting this waveform into Faraday's and Ampere's laws:

$$k_0 \mathbf{n} \times \mathbf{E} = \omega \mathbf{B} \tag{A.2a}$$

$$k_0 \mathbf{n} \times \mathbf{B} = -\omega \mu_0 \tilde{\epsilon} \mathbf{E} \tag{A.2b}$$

Note that the $\mathbf{J}$ term in Ampere's law has been taken into account by using a complex ϵ denoted by $\tilde{\epsilon}$. $\tilde{\epsilon}$ may be found by expressing $\mathbf{J}$ in terms of $\mathbf{E}$ as was done

for ordinary and extraordinary modes in Chapter 1.

Now applying the vector identity for the divergence of a cross product and simpifying:

$$\begin{aligned}
\nabla \cdot (\mathbf{n} \times \mathbf{E}) &= \mathbf{E} \cdot (\nabla \times \mathbf{n}) - \mathbf{n} \cdot (\nabla \times \mathbf{E}) \\
\nabla \cdot (\frac{\omega}{k_0}\mathbf{B}) &= \mathbf{E} \cdot (\nabla \times \mathbf{n}) - \mathbf{n} \cdot (ik_0\mathbf{n} \times \mathbf{E}) \\
i\mathbf{n} \cdot (\omega\mathbf{B}) &= \mathbf{E} \cdot (\nabla \times \mathbf{n}) - i\mathbf{n} \cdot (\omega\mathbf{B}) \\
2i\mathbf{n} \cdot (\omega\mathbf{B}) &= \mathbf{E} \cdot (\nabla \times \mathbf{n}) \\
2i\mathbf{n} \cdot (k_0\mathbf{n} \times \mathbf{E}) &= \mathbf{E} \cdot (\nabla \times \mathbf{n}) \\
2ik_0\mathbf{E} \cdot (\mathbf{n} \times \mathbf{n}) &= \mathbf{E} \cdot (\nabla \times \mathbf{n}) \\
0 &= \mathbf{E} \cdot (\nabla \times \mathbf{n}) \qquad \text{(A.3)}
\end{aligned}$$

This shows that the curl of $\mathbf{n}$ is perpendicular to $\mathbf{E}$. The vector algebra can be repeated using $\mathbf{B}$ to show that $\mathbf{B}$ is perpendicular to the curl of $\mathbf{n}$ as well. But $\mathbf{n}$ must also be perpendicular to the curl of $\mathbf{n}$. This implies that $\mathbf{n}$, $\mathbf{E}$, and $\mathbf{B}$ are coplanar which contradicts Equations A.2a and A.2b. Thus, the only possibility is that one of the four vectors is the zero vector. Since $\mathbf{n}$, $\mathbf{E}$, and $\mathbf{B}$ are not zero, $\nabla \times \mathbf{n} = 0$.

A.2 Key Principle in Ray Tracing

(Adapted from Section 5.3 of [4])

In a loss free plasma where $\mathbf{n}$ is Hermitian, the wave propagates in the direction perpendicular to the refractive index surface. To see this, consider two waves located at the same point: one with refractive index $\mathbf{n}$ and one with refractive index $\mathbf{n} + \delta\mathbf{n}$. The difference between these waves can be quantified by taking the derivative of Equations A.2a and A.2b:

$$\mathbf{n} \times \delta\mathbf{E} + \delta\mathbf{n} \times \mathbf{E} = c[\delta\mathbf{B}] \tag{A.4a}$$

$$\mathbf{n} \times \delta\mathbf{B} + \delta\mathbf{n} \times \mathbf{B} = -c\mu_o\tilde{\epsilon}[\delta\mathbf{E}] \tag{A.4b}$$

Dotting Equation A.4a with $\mathbf{B}^*$ and rearranging terms:

$$\begin{aligned} \mathbf{B}^* \cdot [\mathbf{n} \times \delta\mathbf{E} + \delta\mathbf{n} \times \mathbf{E}] &= c\mathbf{B}^* \cdot \delta\mathbf{B} \\ \delta\mathbf{n} \cdot [\mathbf{E} \times \mathbf{B}^*] &= c\mathbf{B}^* \cdot \delta\mathbf{B} + \delta\mathbf{E} \cdot [\mathbf{n} \times \mathbf{B}^*] \end{aligned} \tag{A.5}$$

Dotting Equation A.4b with $\mathbf{E}^*$ and rearranging terms:

$$\begin{aligned} \mathbf{E}^* \cdot [\mathbf{n} \times \delta\mathbf{B} + \delta\mathbf{n} \times \mathbf{B}] &= -c\mu_o\tilde{\epsilon}\mathbf{E}^* \cdot \delta\mathbf{E} \\ \delta\mathbf{n} \cdot [\mathbf{E}^* \times \mathbf{B}] &= c\mu_o\tilde{\epsilon}\mathbf{E}^* \cdot \delta\mathbf{E} - \delta\mathbf{B} \cdot [\mathbf{n} \times \mathbf{E}^*] \end{aligned} \tag{A.6}$$

Adding together Equations A.5 and A.6:

$$\delta\mathbf{n} \cdot 2Re[\mathbf{E}^* \times \mathbf{B}] = \delta\mathbf{E} \cdot [\mathbf{n} \times \mathbf{B}^* + c\mu_o\tilde{\epsilon}\mathbf{E}^*] - \delta\mathbf{B} \cdot [\mathbf{n} \times \mathbf{E}^* - \mathbf{cB}^*] \tag{A.7}$$

Now the expressions inside of the square brackets on the right are given by the complex conjugates of Equations A.2a and A.2b provided that $\mathbf{n}$ is Hermitian. Therefore:

$$\delta\mathbf{n} \cdot Re[\mathbf{E}^* \times \mathbf{B}] = 0 \tag{A.8}$$

Since the Poynting Vector is proportional to $Re[\mathbf{E}^* \times \mathbf{B}]$, this means that $\delta\mathbf{n}$ is perpendicular to the direction of wave propagation. Since the two waves described at the start of the derivation have the same spacial coordinates, they are on the

same refractive index surface in n-space. This means that $\delta\mathbf{n}$ must point along the surface; thus by Equation A.8 the wave propagation direction is perpendicular to the refractive index surface in n-space.

Appendix B

Ray Tracing Code

What follows is the ray tracing code used to model naturally occurring ionospheric ducts and construct refractive index surface plots. The modeling was done in Mathematica and is an extension of the code written by Nathan Dalrymple [1].

B.1 Code Modified for Ducts

First, we set up the Mathematica environment:

```
Off[General::spell1]
$TextStyle = {FontSize → 12, FontFamily → "Times"}
<< Graphics`Colors`
<< Graphics`Arrow`
```

{FontSize → 12, FontFamily → Times}

Next, we define the Appleton-Hartree dispersions relations for X and O modes:

```
nor[r_, n_, f_]:=
√(1 - (X[r, f](1 - X[r, f]))/
(-½Y[f].Y[f](Sin[Θ[Y, n, f]])²+
√(¼(Y[f].Y[f])²(Sin[Θ[Y, n, f]])⁴ + (Cos[Θ[Y, n, f]])²Y[f].Y[f](1 - X[r, f])²) - X[r, f] + 1))
nex[r_, n_, f_]:=
√(1 - (X[r, f](1 - X[r, f]))/
(-½Y[f].Y[f](Sin[Θ[Y, n, f]])²-
```

$$\sqrt{(\tfrac{1}{4}(Y[f].Y[f])^2(\mathrm{Sin}[\Theta[Y,n,f]])^4+(\mathrm{Cos}[\Theta[Y,n,f]])^2Y[f].Y[f](1-X[r,f])^2)-X[r,f]+1)}$$

$$\mathrm{Gor}[r\_,n\_,f\_]:=\frac{\sqrt{n.n}}{\mathrm{nor}[r,n,f]}$$

$$\mathrm{Gex}[r\_,n\_,f\_]:=\frac{\sqrt{n.n}}{\mathrm{nex}[r,n,f]}$$

$$\mathrm{Gor}[z[s],n,f]$$

$$\mathrm{Gex}[z[s],n,f]$$

$$\frac{\sqrt{n.n}}{\sqrt{1-\frac{(1-X[z[s],f])X[z[s],f]}{1-\frac{1}{2}Y[f].Y[f]\mathrm{Sin}[\Theta[Y,n,f]]^2+\sqrt{\frac{1}{4}(Y[f].Y[f])^2\mathrm{Sin}[\Theta[Y,n,f]]^4+\mathrm{Cos}[\Theta[Y,n,f]]^2Y[f].Y[f](1-X[z[s],f])^2}-X[z[s],f]}}}$$

$$\frac{\sqrt{n.n}}{\sqrt{1-\frac{(1-X[z[s],f])X[z[s],f]}{1-\frac{1}{2}Y[f].Y[f]\mathrm{Sin}[\Theta[Y,n,f]]^2-\sqrt{\frac{1}{4}(Y[f].Y[f])^2\mathrm{Sin}[\Theta[Y,n,f]]^4+\mathrm{Cos}[\Theta[Y,n,f]]^2Y[f].Y[f](1-X[z[s],f])^2}-X[z[s],f]}}}$$

The following commands set up the declination angle and strength of the magnetic field. Y is a vector whose magnitude is the ratio of the electron cyclotron frequency to the frequency transmitted and whose direction is that of the magnetic field.

$$\Theta[Y\_,n\_,f\_]:=\mathrm{ArcCos}[\frac{Y[f].n}{\sqrt{Y[f].Y[f]n.n}}]$$

$$\theta\mathrm{Div}=47.5\mathrm{Degree};$$

$$\mathrm{fce}=0.810^6;$$

$$Y[f\_]:=\frac{\mathrm{fce}}{f}\{-\mathrm{Cos}[\theta\mathrm{Div}],0,\mathrm{Sin}[\theta\mathrm{Div}]\}$$

These commands define several important fundamental parameters. The ionosphere is set up as a Chapman layer and the magnetic ducts are modeled in the xz plane using the sinusoidal form $\delta n[r]$.

$$\mathrm{ne}[r\_]:=\mathrm{ne0}e^{\frac{1}{2}(-\frac{r[[3]]-z0}{H}-\mathrm{Sec}[\chi]e^{-\frac{r[[3]]-z0}{H}}+1)}$$

$$\delta\mathrm{n}[r\_]:=\delta\mathrm{n0}\mathrm{Sin}[\frac{2\pi}{d}(r[[3]]\mathrm{Cos}[\theta\mathrm{Div}]+r[[1]]\mathrm{Sin}[\theta\mathrm{Div}])]$$

$$X[r\_,f\_]:=\frac{e^2\mathrm{ne}[r](1+\delta\mathrm{n}[r])}{\epsilon0\mathrm{me}(2\pi f)^2}$$

$$\chi=0;$$

$$\mathrm{z0}=250;$$

$$H=40;$$

$$\mathrm{ne0}=13000010^6;$$

$$e=\frac{1.602}{10^{19}};$$

$$\epsilon0=\frac{8.854}{10^{12}};$$

$$\mathrm{me}=\frac{0.91}{10^{30}};$$

$$\mathrm{f0}=3.17510^6;$$

$$\delta\mathrm{n0}=210^{-2};$$

$d = 0.3;$

chapPlot = ParametricPlot[{X[{0, 0, z}, f0], z}, {z, 0, 400}, PlotRange → {{0, 1.2}, {0, 400}},
GridLines → Automatic, Frame → Automatic,
FrameLabel → {"$\frac{\omega_{pe}^2}{\omega^2}$", "Altitude(km)", "Chapman layer used in ray tracing", ""},
RotateLabel → False, AspectRatio → 1.2]

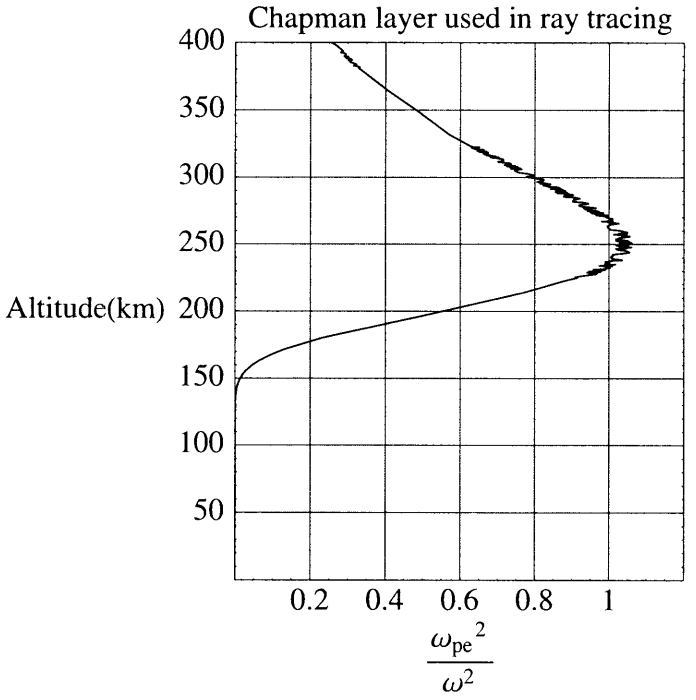

–Graphics–

Critical angle that defines the boundary between cusps at the reflection height (small angles) and a smooth path (large angles) for a quiet ionosphere.

$$\theta_c = \frac{\text{ArcSin}[\sqrt{\frac{\sqrt{Y[f0].Y[f0]}}{\sqrt{Y[f0].Y[f0]}+1}}\,\text{Sin}[42.5\text{Degree}]]}{1\text{Degree}}$$

17.6428

Angle by which the ray deviates from the meridional plane. This is set to a small number to prevent the ray tracing equations from failing due to singularities.

$\beta = 0.0015$

0.0015

The crux of the code; defines how much to step in both frequency and angle and then

solves the ray tracing equations for the given parameters. Note: this code may use up all of the memory on a machine if too many steps are chosen at once, causing that computer to crash. To get around this problem, choose a reasonable step size and then contract the vectors corddisp and cextdisp from the different runs and display them on a single ionogram.

$\theta\text{min} = -5\text{Degree};$

$\theta\text{max} = 5\text{Degree};$

$\theta\text{step} = 0.5\text{Degree};$

$\text{fmin} = 1.037310^6;$

$\text{fmax} = 3.237310^6;$

$\text{fstep} = 0.210^6;$

$\text{freqvals} = \text{Table}[\frac{f}{10^6}, \{f, \text{fmin}, \text{fmax}, \text{fstep}\}];$

$\text{smax} = 1000;$

$\text{ordSol} = \text{Flatten}[\text{Table}[\text{NDSolve}[$

$\{x'[s] == D[\text{Gor}[\{x[s], y[s], z[s]\}, \{\text{nx}[s], \text{ny}[s], \text{nz}[s]\}, b], \text{nx}[s]],$

$y'[s] == D[\text{Gor}[\{x[s], y[s], z[s]\}, \{\text{nx}[s], \text{ny}[s], \text{nz}[s]\}, b], \text{ny}[s]],$

$z'[s] == D[\text{Gor}[\{x[s], y[s], z[s]\}, \{\text{nx}[s], \text{ny}[s], \text{nz}[s]\}, b], \text{nz}[s]],$

$\text{nx}'[s] == -D[\text{Gor}[\{x[s], y[s], z[s]\}, \{\text{nx}[s], \text{ny}[s], \text{nz}[s]\}, b], x[s]],$

$\text{ny}'[s] == -D[\text{Gor}[\{x[s], y[s], z[s]\}, \{\text{nx}[s], \text{ny}[s], \text{nz}[s]\}, b], y[s]],$

$\text{nz}'[s] == -D[\text{Gor}[\{x[s], y[s], z[s]\}, \{\text{nx}[s], \text{ny}[s], \text{nz}[s]\}, b], z[s]],$

$x[0] == 0, y[0] == 0, z[0] == 0, \text{nx}[0] == \text{Sin}[a],$

$\text{ny}[0] == \beta, \text{nz}[0] == \text{Sqrt}[1 - (\text{nx}[0]^2 + \text{ny}[0]^2)]\},$

$\{x[s], y[s], z[s], \text{nx}[s], \text{ny}[s], \text{nz}[s]\},$

$\{s, 0, \text{smax}\}, \text{MaxSteps} \rightarrow \text{Infinity}], \{a, \theta\text{min}, \theta\text{max}, \theta\text{step}\}, \{b, \text{fmin}, \text{fmax}, \text{fstep}\}], 1];$

$\text{extSol} = \text{Flatten}[\text{Table}[\text{NDSolve}[$

$\{x'[s] == D[\text{Gex}[\{x[s], y[s], z[s]\}, \{\text{nx}[s], \text{ny}[s], \text{nz}[s]\}, b], \text{nx}[s]],$

$y'[s] == D[\text{Gex}[\{x[s], y[s], z[s]\}, \{\text{nx}[s], \text{ny}[s], \text{nz}[s]\}, b], \text{ny}[s]],$

$z'[s] == D[\text{Gex}[\{x[s], y[s], z[s]\}, \{\text{nx}[s], \text{ny}[s], \text{nz}[s]\}, b], \text{nz}[s]],$

$\text{nx}'[s] == -D[\text{Gex}[\{x[s], y[s], z[s]\}, \{\text{nx}[s], \text{ny}[s], \text{nz}[s]\}, b], x[s]],$

$\text{ny}'[s] == -D[\text{Gex}[\{x[s], y[s], z[s]\}, \{\text{nx}[s], \text{ny}[s], \text{nz}[s]\}, b], y[s]],$

```
nz'[s] == -D[Gex[{x[s], y[s], z[s]}, {nx[s], ny[s], nz[s]}, b], z[s]],
x[0] == 0, y[0] == 0, z[0] == 0, nx[0] == Sin[a],
ny[0] == β, nz[0] == Sqrt[1 - (nx[0]^2 + ny[0]^2)]},
{x[s], y[s], z[s], nx[s], ny[s], nz[s]},
{s, 0, smax}, MaxSteps → Infinity], {a, θmin, θmax, θstep}, {b, fmin, fmax, fstep}], 1];

pxmin = -100;
pxmax = 100;
pymax = 250;

pasp = pymax/(pxmax - pxmin)
```

$\frac{5}{4}$

Determines the value of s (psordgnd) and x (pxordgnd) at which each O mode ray traced returns to the ground and then constructs a table listing the frequency, effective altitude (s/2), and distance from the transmitter (x) for each ray. The paths of all the rays are then plotted.

```
psordgnd = s/.Table[FindRoot[Evaluate[z[s]/.ordSol[[a, 1]]] == 0,
{s, 300, smax}], {a, 1, Dimensions[ordSol][[1]]}];
pxordgnd = Table[x[s]/.ordSol[[a, 1]], {a, 1, Dimensions[ordSol][[1]]}, {s, psordgnd[[a]],
psordgnd[[a]]}];
cordgnd = Table[{freqvals[[Mod[a - 1, Dimensions[freqvals][[1]]] + 1]], psordgnd[[a]]/2,
pxordgnd[[a]][[1]]}, {a, 1, Dimensions[ordSol][[1]]}]
ordPlot =
Show[{Table[ParametricPlot[Evaluate[{x[s], z[s]}/.ordSol[[a, 1]]],
{s, 0, psordgnd[[a]]}, PlotRange → {{pxmin, pxmax}, {0, pymax}},
AspectRatio → pasp, DisplayFunction → Identity, PlotStyle → Red],
{a, 1, Dimensions[ordSol][[1]]}]},
DisplayFunction → $DisplayFunction]
```

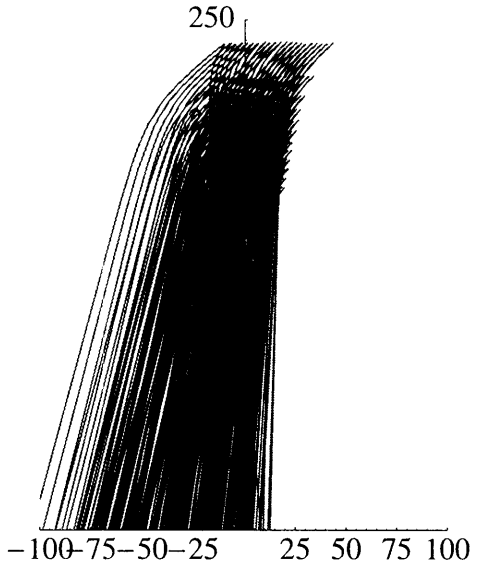

−Graphics−

pfmin = 0;

pfmax = 4;

phmax = 250;

Selects only those rays which return to ground within one kilometer of the transmitter and plots them on an ionogram.

corddisp = Select[cordgnd, Abs[#[[3]]] < 1&]

zordplot = ListPlot[Table[{corddisp[[a]][[1]], corddisp[[a]][[2]]}, {a, 1, Dimensions[corddisp][[1]]}], PlotRange → {{pfmin, pfmax}, {0, phmax}}, PlotStyle → Red]

{{3.0373, 207.062, 0.705481}, {2.2373, 187.112, 0.65332}, {1.4373, 172.459, 0.941904}, {1.0373, 164.824, −0.269159}, {2.4373, 191.722, 0.298675}, {2.6373, 196.103, −0.733157}, {2.8373, 200.923, 0.560243}, {2.0373, 183.989, 0.87263}, {3.0373, 206.995, −0.742078}}

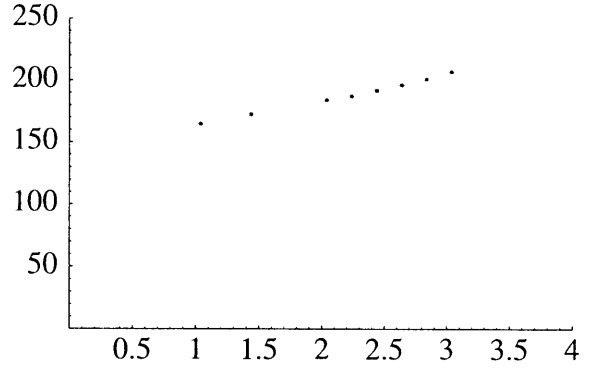

−Graphics−

Repeats the process outlined above for X mode waves.

```
psextgnd = s/.Table[FindRoot[Evaluate[z[s]/.extSol[[a, 1]]] == 0,
{s, 250, smax}], {a, 1, Dimensions[extSol][[1]]}];
pxextgnd = Table[x[s]/.extSol[[a, 1]], {a, 1, Dimensions[extSol][[1]]}, {s, psextgnd[[a]], psextgnd[[a]]}];
cextgnd = Table[{freqvals[[Mod[a − 1, Dimensions[freqvals][[1]]] + 1]], psextgnd[[a]]/2,
pxextgnd[[a]][[1]]}, {a, 1, Dimensions[extSol][[1]]}]
extPlot =
Show[{Table[ParametricPlot[Evaluate[{x[s], z[s]}/.extSol[[a, 1]]],
{s, 0, psextgnd[[a]]}, PlotRange → {{pxmin, pxmax}, {0, pymax}},
AspectRatio → pasp, DisplayFunction → Identity,
PlotStyle → {Blue, Dashing[{0.03, 0.02}]}],
{a, 1, Dimensions[extSol][[1]]}]},
DisplayFunction → $DisplayFunction]
cextdisp = Select[cextgnd, Abs[#[[3]]] < 1&]
zextplot = ListPlot[Table[{cextdisp[[a]][[1]], cextdisp[[a]][[2]]}, {a, 1, Dimensions[cextdisp][[1]]}],
PlotRange → {{pfmin, pfmax}, {0, phmax}}, PlotStyle → Blue]
```

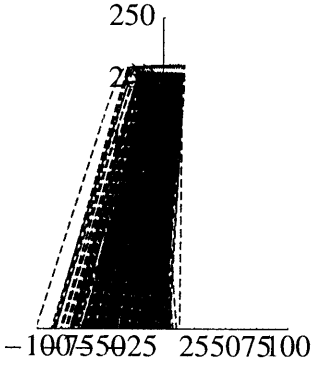

−Graphics−

{{2.4373, 181.938, 0.431969}, {2.2373, 177.986, 0.974249},
{2.8373, 189.172, 0.271794}, {2.8373, 189.092, −0.957528}, {1.0373, 151.111, −0.839944}}

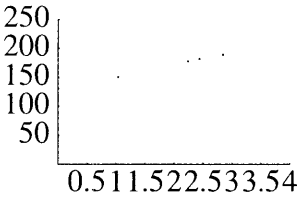

−Graphics−

Plots both X and O mode results on the same graph.

igram = Show[{zordplot, zextplot}]

Syntax::noinfo : Input expression contains insufficient information to interpret result. More...

−Graphics−

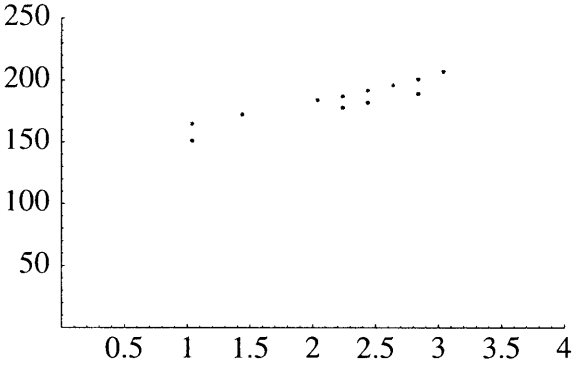

−Graphics−

B.2 Refractive Index Surface Plots

First, we set up the Mathematica environment:

```
Off[General::spell1]
$TextStyle = {FontSize → 12, FontFamily → "Times"}
<< Graphics`Colors`
<< Graphics`Arrow`
<< Graphics`ImplicitPlot`
nor[n_, X_]:=√(1 − (X(1 − X))/(−½Y.Y(Sin[Θ[Y, n]])²+
√(¼(Y.Y)²(Sin[Θ[Y, n]])⁴ + (Cos[Θ[Y, n]])²Y.Y(1 − X)²) − X + 1))
nex[n_, X_]:=√(1 − (X(1 − X))/(−½Y.Y(Sin[Θ[Y, n]])²−
√(¼(Y.Y)²(Sin[Θ[Y, n]])⁴ + (Cos[Θ[Y, n]])²Y.Y(1 − X)²) − X + 1))
Gor[n_, X_]:=√n.n / nor[n,X]
Gex[n_, X_]:=√n.n / nex[n,X]
Gor[n[s], X]
Gex[n[s], X]
```

{FontSize → 12, FontFamily → Times}

Next, we define the Appleton-Hartree dispersions relations for X and O modes as well as the declination angle and strength of the magnetic field. Y is a vector whose magnitudes is the ratio of the electron cyclotron frequency to the frequency transmitted and whose direction is that of the magnetic field. Cutoff frequencies are also defined.

$$\frac{\sqrt{n[s].n[s]}}{\sqrt{1-\frac{(1-X)X}{1-X-\frac{1}{2}Y.Y\,\mathrm{Sin}[\Theta[Y,n[s]]]^2+\sqrt{(1-X)^2\mathrm{Cos}[\Theta[Y,n[s]]]^2Y.Y+\frac{1}{4}(Y.Y)^2\mathrm{Sin}[\Theta[Y,n[s]]]^4}}}}$$

$$\frac{\sqrt{n[s].n[s]}}{\sqrt{1-\frac{(1-X)X}{1-X-\frac{1}{2}Y.Y\,\mathrm{Sin}[\Theta[Y,n[s]]]^2-\sqrt{(1-X)^2\mathrm{Cos}[\Theta[Y,n[s]]]^2Y.Y+\frac{1}{4}(Y.Y)^2\mathrm{Sin}[\Theta[Y,n[s]]]^4}}}}$$

```
Θ[Y_, n_]:=ArcCos[Y.n / √Y.Y n.n]
θDiv = 47.5Degree;
Y = 0.3334{−Cos[θDiv], 0, Sin[θDiv]}
cut1 = 1 − √Y.Y;
cut2 = 1 − Y.Y;
cut3 = 1 + √Y.Y;
```

$\{-0.225242, 0, 0.245808\}$

Plots refractive index surfaces in the magnetic meridian plane for ordinary mode from the ground (outer circle) to near the O mode reflection height.

ordeqns = Table[Gor[{nx, 0, nz}, XX] == 1, {XX, 0, 0.99, 0.11}];
ordsurfs = ImplicitPlot[ordeqns, {nx, −1, 1}, {nz, −1, 1}, AxesLabel → {n_x, n_z}]

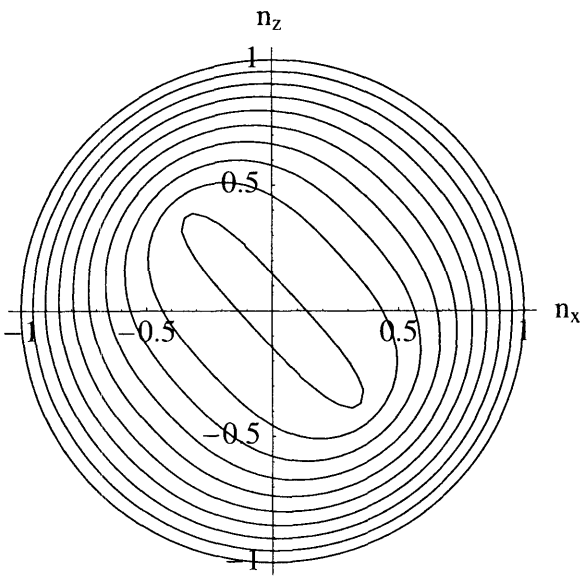

−Graphics−

Plots refractive index surfaces perpendicular to the magnetic meridian plane for ordinary mode from the ground (outer circle) to near the O mode reflection height.

ordeqns2 = Table[Gor[{0, ny, nz}, XX] == 1, {XX, 0, 0.99, 0.11}];
ordsurfs2 = ImplicitPlot[ordeqns2, {ny, −1, 1}, {nz, −1, 1}, AxesLabel → {n_y, n_z}]

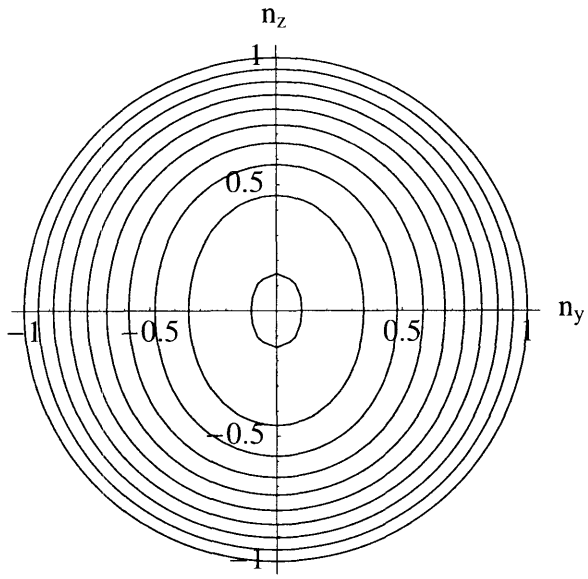

−Graphics−

Plots refractive index surfaces in the magnetic meridian plane for extraordinary mode from the ground (outer circle) to near the X mode reflection height (right hand cutoff).

exteqns = Table[Gex[{nx, 0, nz}, XX] == 1, {XX, 0, cut1, 0.05}];

extsurfs = ImplicitPlot[exteqns, {nx, −1, 1}, {nz, −1, 1}, AxesLabel → {n_x, n_z}]

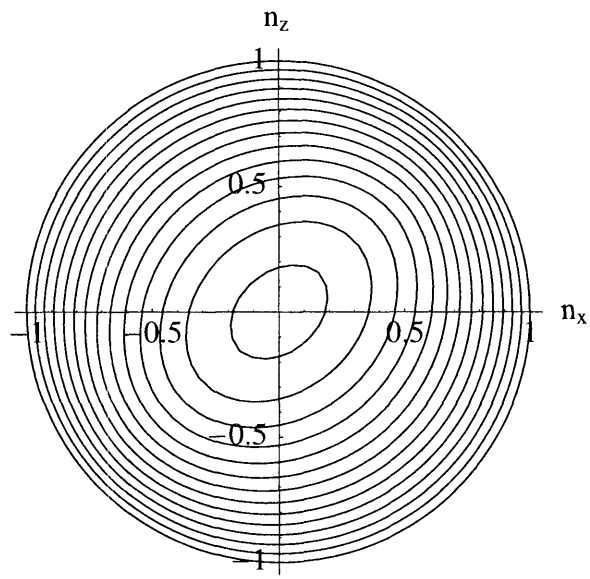

−Graphics−

Plots refractive index surfaces in the magnetic meridian plane for extraordinary mode from the upper hybrid frequency to near the left hand cutoff.

exteqns2 = Table[Gex[{nx, 0, nz}, XX] == 1, {XX, cut2 + 0.01, cut3, 0.01}];

extsurfs2 = ImplicitPlot[exteqns2, {nx, −1, 1}, {nz, −1, 1}]

ContourGraphics::ctpnt : The contour is attempting to traverse a

cell in which some of the points have not evaluated to numbers, and it will be dropped. More...

ContourGraphics::ctpnt : The contour is attempting to traverse a

cell in which some of the points have not evaluated to numbers, and it will be dropped. More...

ContourGraphics::ctpnt : The contour is attempting to traverse a

cell in which some of the points have not evaluated to numbers, and it will be dropped. More...

General::stop : Further output of ContourGraphics::ctpnt will be suppressed during this calculation. M

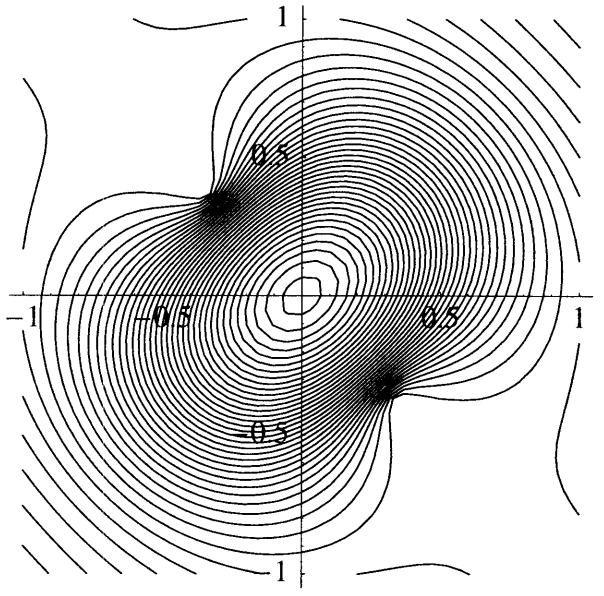

−Graphics−

Sets up a different magnetic field such that the transmitted frequency is less than the

electron cyclotron frequency.

θDiv = 47.5Degree;

Y = 3{−Cos[θDiv], 0, Sin[θDiv]}

cut4 = 1 + $\sqrt{Y.Y}$;

{−2.02677, 0, 2.21183}

Plots refractive index surfaces in the magnetic meridian plane for extraordinary mode

under the new circumstances.

exteqns3 = Table[Gex[{nx, 0, nz}, XX] == 1, {XX, 0, 0.99, 0.11}];

extsurfs3 = ImplicitPlot[exteqns3, {nx, −1, 1}, {nz, −1, 1}, AxesLabel → {n_x, n_z}]

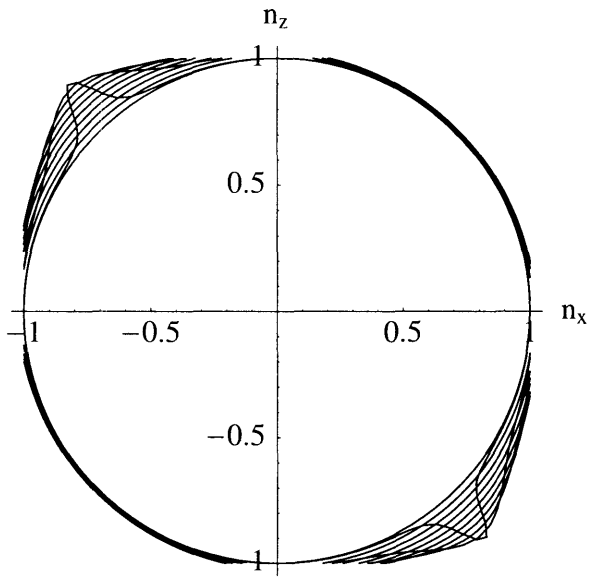

−Graphics−

exteqns4 = Table[Gex[{nx, 0, nz}, XX] == 1, {XX, 1.01, cut4, 0.11}];

extsurfs4 = ImplicitPlot[exteqns4, {nx, −1, 1}, {nz, −1, 1}, AxesLabel → {n_x, n_z}]

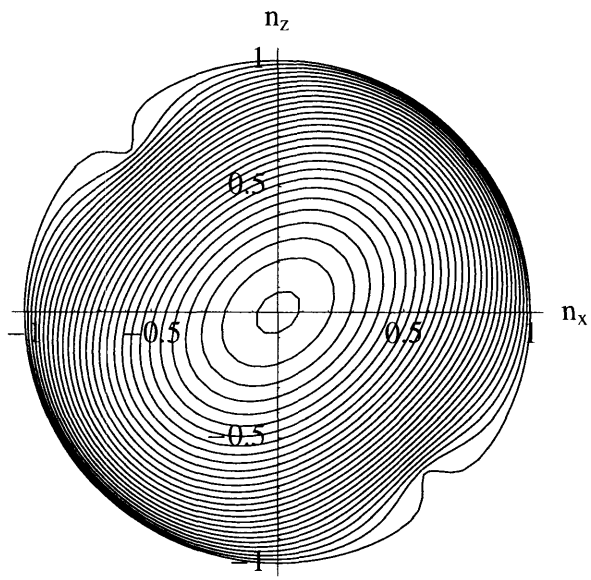

−Graphics−